Nonlinear Damping Dynamics and the Variability of Rapid Aimed Movements

Michael Kositsky   Andrew G. Barto

{kositsky, barto}@cs.umass.edu

Abstract

This report describes a set of computational experiments aimed at studying movement variability and speed-accuracy trade-off relationships for dynamic models with nonlinear damping. We analyzed ballistic movements with noisy control signals and noisy plant dynamics. Most of the theories suggested so far to explain observed speed-accuracy relationships are purely kinematic and do not take into consideration the dynamic behavior of the system in question. A dynamic model with fractional-power damping is motivated by biological evidence and allows a completely new view of the speed-accuracy trade-off phenomenon. This model gives rise to a dynamic behavior called a stiction region.

Data obtained from our simulations make a good fit with the linear speed-accuracy relationship model. The speed-accuracy relationship critically depends on the proportion of movements that hit the inner area of the stiction region versus the proportion of movements that undershoot or overshoot the region, thereby effectively stopping on an edge of the region. These results provide a new perspective on possible mechanisms for both the linear and logarithmic speed-accuracy relationships observed in reaching.

1 Introduction

Properties of rapid aimed movements have been studied for more than a century. One of the most interesting aspects of rapid movements is their variability and the so-called speed-accuracy trade-off. One of the earliest works in this field is by Woodworth (1899). Since then many different researchers have provided experimental data on this issue as well as various explanations and theories. Some of the explanations suggested so far involve sensory feedback processing during the movement and rely on complex computations being performed by the nervous system. These can be referred to as closed-loop variability models. Other theories suggest that the observed speed-accuracy relationship is a product of dynamic properties of the nervous system, muscles, and the mechanical system being moved. These can be referred to as open-loop variability models. Both closed-loop and the open-loop factors contribute to the observed speed-accuracy relationship. This paper analyses a certain class of open-loop variability models.

Most of the theories suggested so far to explain observed speed-accuracy relationships are purely kinematic; they do not take into consideration dynamic behavior of the system in question. Dynamic models with linear damping do not leave much space for final position variability, at least in the case of purely ballistic movements. The final position variability is the same as the corresponding control signal variability. This is not the case, though, for dynamic models with nonlinear damping. A dynamic model with fractional-power damping is motivated by biological evidence and allows a completely new view of the speed-accuracy trade-off phenomenon.

We studied simulated movements using a second-order linear dynamic system with fractional-power damping (Wu *et al.*, 1990):

$$m\ddot{x} + b\dot{x}^{\frac{1}{5}} + k\left(x - u\right) = 0. \tag{1}$$

The fractional-power damping term models the dynamics of spinal reflex circuitry (Houk *et al.*, 2001), and it turns out to create qualitatively novel dynamic features that may be critical to understanding the variability of rapid movements. The most important feature in this context is the so-called "stiction" region (Houk *et al.*, 2001). The stiction region is an extended region in the state space where, for certain fixed control signals, the plant "sticks", i.e., effectively stops. For each fixed control signal the stiction region has well-defined borders. A stiction region is similar to a stable equilibrium position for a spring-mass system with linear damping. A stiction region spans an extended range of the position axis as opposed to a stable equilibrium point.

Any final position variability can only take place within the stiction region. This consideration introduces a completely new perspective onto the issue of variability of rapid movements. For a set of movements, the speed-accuracy relationship critically depends on whether all movements terminate in the inner area of the stiction region, or some of the movements first undershoot or overshoot the stiction region and terminate at the near or far edge of it.

We analyzed only ballistic movements of system (1) without any learning or feedback processing. The control signal for each of the movements was in the form of a pulse-step combination (Robinson, 1975; Ghez, 1979; Ghez and Martin, 1982; Gottlieb, 1993). Series of movements were simulated with noisy parameters of the pulse-step combination, or noisy plant dynamics. Each movement continued until the plant came to an effective stop, and final position distributions as well as movement times and velocities for each of the sets were analyzed.

The data obtained can account for different kinds of speed-accuracy relationships described in the corresponding experimental literature. The data provide a new interpretation of one of

the controversies in the speed-accuracy literature: the logarithmic versus linear speed-accuracy relationship. Considerable evidence suggests a logarithmic speed-accuracy relationship called Fitts' law (see, e.g., Fitts, 1954; Crossman and Goodeve, 1983; Kvalseth, 1975), but other evidence suggests a linear speed-accuracy relationship (e.g., Schmidt *et al.*, 1979; Zelaznik *et al.*, 1981; Wright and Meyer, 1983).

One of many possible explanations of the logarithmic versus linear relationship controversy is the way the movement times, movement amplitudes, and average velocities are computed. When data are represented in terms of Fitts' law the movement times should be averaged over a set of movements separately from movement amplitudes. However when data are represented in terms of the linear relationship (e.g., as in Schmidt *et al.*, 1979) average velocity of each particular movement can be computed and then an average of all the velocities can be computed. In the general case these two representations produce different results.

Our simulations produce data that make a good fit with the linear relationship model. We also show that for some movements different results are produced by the two representations for speed and accuracy described in the preceding paragraph. This happens for series of movements where some of the movements undershoot or overshoot the stiction region and slowly drift toward its edge. These series of movements produce data that make a good fit with the logarithmic as well as with the linear relationship in a manner we describe below.

The next section describes the relevant experimental evidence as well as some of the theories and speculations on the issue. Section 3 describes the dynamical model used in the simulations and the biological motivation for the model. Section 4 explains why the stiction region emerges and describes the relevant dynamic properties and movement features determined by the stiction region. Section 5 describes the exact experimental paradigm used in the simulations and alternative models of noise injection into the control signal and into the plant dynamics. Section 6 describes the results of the computational experiments. Discussion of the results and their possible interpretations are provided in Section 7.

2   Speed-accuracy relationship evidence and theories

This section provides a brief review of speed-accuracy trade-off evidence and theories. A comprehensive review and discussion of these issues is provided by Plamondon and Alimi (1997).

One of the most famous theories suggesting a quantitative description of the observed speed-accuracy relationship for rapid movements is Fitts' law (Fitts, 1954):

$$MT = a + b \log_2 \left(\frac{2A}{W} \right). \tag{2}$$

Here MT is the movement time, A is the movement amplitude, W is the so-called effective target width, and a and b are the regression coefficients. In Fitts' experiments subjects were asked to tap alternately two target stripes with a stylus. The targets were set on a table and their width and the distance between them were varied for different sets of trials. Subjects were asked to tap the targets as fast as possible while hitting within the specified target regions. The logarithmic term in (2) was called by Fitts (1954) index of difficulty:

$$ID = \log_2 \left(\frac{2A}{W} \right).$$

2

The index of difficulty determines how difficult a certain task is, which depends on the distance to the target A and the required accuracy W. Equation (2) defines how much time is required to accomplish a task depending on its index of difficulty. Equation (2) was formulated by Crossman and Goodeve (1983). Although Fitts' law has drawn some criticism and counter-evidence, it was re-confirmed by various experimental studies (see, e.g., Crossman, 1956; Crossman and Goodeve, 1983; Kvalseth, 1975; Jagacinski *et al.*, 1980; Jagacinski and Monk, 1985; Corcos *et al.*, 1988; Brooks, 1979).

Numerous theories and models have been put forward for how Fitts' law could be produced. Some of the models are biologically plausible, while others only provide pure theoretical foundations. One of the most famous theories was suggested by Crossman and Goodeve (1983) and was developed later by Keele (1968) and Langolf *et al.* (1976). This is the iterative corrections theory. According to this theory, each movement is accomplished by a series of sub-movements. Each sub-movement takes fixed time t and reduces the distance to the target by a fixed fraction p. Starting at distance A from the target and finishing the last sub-movement at distance $\frac{W}{2}$ from the target center yields (2). Coefficients a and b in (2) in this case are determined by t and p. The iterative corrections theory has drawn much support in the literature. One of the main criticisms of this theory is that it relies heavily on feedback processing which takes quite a long time, sometimes the same order of magnitude or even longer than a typical movement duration.

A modification of the iterative corrections theory was suggested by Connelly (1984). This theory is based on the assumption that the remaining distance to the target decreases exponentially and its time derivative is proportional to the negative remaining distance. This assumption yields the same expression (2) for Fitts' law. Actually it is another version of the iterative corrections theory where corrections occur continuously in time.

Among other theories for Fitts' law there should be mentioned the unifying noise-velocity relationship theory of Chan and Childress (1990), the stochastic optimized submovement model suggested by Meyer *et al.* (1988) (see also Meyer *et al.* (1990)), the VITE (vector-integration-to-endpoint) model of Bullock and Grossberg (1988), and the kinematic theory of Plamondon (1995a, 1995b).

Another set of theories advocates a linear speed-accuracy relationship rather than the logarithmic one suggested by Fitts' law. Evidence for the linear relationship was first provided by Schmidt *et al.* (1979). They formulate the relationship in terms of the following equation:

$$W = c + d\frac{A}{MT},\tag{3}$$

where W, A, and MT denote the target width, the movement amplitude, and the movement time exactly as in (2), and the term $\frac{A}{MT}$ is the average velocity of the movement. Although the literature on the linear relationship is not as voluminous as the one on Fitts' law, there exists considerable evidence supporting this hypothesis (Zelaznik *et al.*, 1981; Zelaznik *et al.*, 1988; Meyer *et al.*, 1982; Wright, 1983; Wright and Meyer, 1983; Meyer *et al.*, 1988; Abrams *et al.*, 1989).

One of the main theories explaining the linear speed-accuracy relationship was first suggested by Schmidt *et al.* (1979). According to this theory, noise in the nervous system is proportional to the control signal magnitude, and higher average velocity requires a control signal of higher magnitude, thus causing higher noise magnitude in the control signal and higher variability of the final positions. This explanation works if the movements are executed in a purely feed-forward manner. To ensure this, Schmidt *et al.* (1979) forced subjects to accomplish movements in less than 500 ms to rule out possible visual feedback processing. However, this explanation has several weak points. As

Schmidt et al. (1979) note themselves, their reasoning yields a proportional relationship and not just a linear relationship, i.e., the relationship should have zero intercept. The data, in contrast, suggest a non-zero intercept. Schmidt et al. (1979) explain this by a tremor always produced by the nervous system. Another weak point of this explanation is that visual feedback is not the only feedback used to produce corrections in the middle of movements. There is quite strong evidence (see, e.g., Lackner and Dizio, 1994) that proprioceptive feedback suffices to produce very accurate movements, and the delay for proprioceptive feedback is much shorter than 500 ms.

Other researchers (Wright and Meyer, 1983; Meyer et al., 1988; Zelaznik et al., 1988) investigated what other movement parameters or circumstances apart from short movement times determine the linear speed-accuracy relationship. They found that when subjects were required to produce movements with much temporal accuracy, the linear relationship was observed very clearly even for movements of long durations (much longer than 500 ms). When only the spatial accuracy was required, a Fitts' law kind of relationship was observed.

We have observed both kinds of relationships in our computational experiments. Discussion of this controversial issue is postponed until Section 7. The next section describes the dynamic model used in our experiments.

3 Nonlinear damping model of plant dynamics

One nonlinear damping dynamics model is the fractional-power damping model suggested by Houk (1981). Further qualitative analysis of the behavior of this model was provided by Wu et al. (1990). This model arises from certain simplifying assumptions about muscle mechanical properties and spinal reflex mechanisms and is suggested by some experimental evidence (e.g. Gielen and Houk, 1984, 1987). The fractional-power damping in the model arises from the interaction of muscle properties and the friction-like property of the stretch reflex. From the experimental data (Miller, 1984; Gielen and Houk, 1987) the damping seems to be proportional to the velocity raised into power of 0.17. This parameter is usually rounded to 1/5 (Wu et al., 1990; Barto et al., 1999; Houk et al., 2001), and the model is called the fractional-power damping model.

The simplest model that captures the above mentioned critical features is a spring-mass system with the fractional-power damping term. The dynamics of the spring-mass system with fractional-power damping is determined by the following equation (Barto et al., 1999):

$$m\ddot{x} + b\dot{x}^{\frac{1}{5}} + k(x - u) = 0. \tag{4}$$

Here x denotes the position of the object attached to the spring, $\dot{x}$ and $\ddot{x}$ denote respectively the velocity and the acceleration of the object, m denotes the mass of the object (the mass of the spring is assumed to be equal to zero), b denotes the damping coefficient, k denotes the stiffness coefficient, u denotes the resting, or equilibrium, position. The equilibrium position is the only parameter used to control the system. Later in this report we call it activation, referring to the activation level of a muscle pair being modeled.

The damping force is always directed opposite to the direction of the movement. In the model being discussed the magnitude of the damping force is proportional to the one-fifth power of the absolute value of the movement velocity. Equation (4) defines the damping term properly only for non-negative velocities $\dot{x}$. The following modification of (4) stands in agreement with the damping force specification for any velocity value:

$$m\ddot{x} + b \cdot \text{sign}(\dot{x}) \cdot |\dot{x}|^{\frac{1}{5}} + k(x - u) = 0. \tag{5}$$

4

The values for the mass, the damping coefficient, and the stiffness coefficient were taken from Barto *et al.* (1999): $m = 1$ kg, $b = 3$ N $\left(\frac{s}{m}\right)^{\frac{1}{5}}$, $k = 30 \frac{N}{m}$. These values provide movement trajectories qualitatively similar to those observed in human wrist movements (Wu *et al.*, 1990). Reasonable amplitudes of typical movements for this system do not exceed 10 cm, and reasonable activation magnitudes (the equilibrium position u) do not exceed 20 cm from the current position, x. Reasonable movement durations for this system would be around or below 600 ms.

A typical movement of the mass with fractional-power damping is shown in Figure 1. The activation signal used to produce this movement consists of two constant phases according to the pulse-step control paradigm described in Section 5. The movement shown in Figure 1, as would any typical movement of system (5) under the pulse-step control, depicts the main qualitative characteristics of the dynamic behavior observed in rapid aimed human movements, but the velocity profile is not similar to what is observed in human movements.
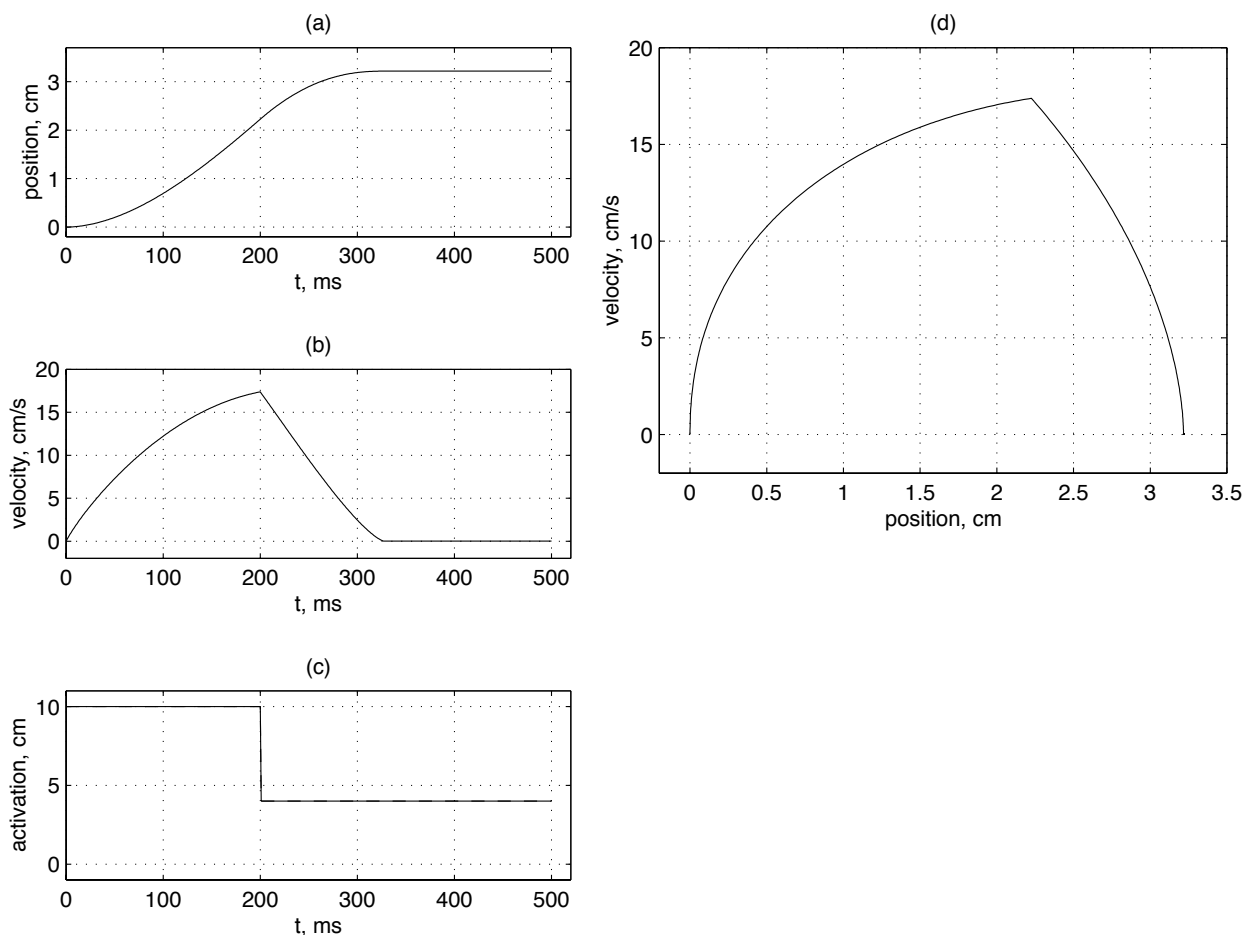
Figure 1: A typical movement of the mass with fractional-power damping. Panels *(a)*, *(b)*, and *(c)* show, respectively, the movement position, velocity, and the control signal as a function of time. Panel *(d)* shows the phase space trajectory of the movement.

One of the most salient properties observed in rapid aimed human movements is a smooth bell-shaped velocity time-course profile, which is not well reproduced by the model (Figure 1*(b)*). A bell-

shaped velocity profile has been observed in multiple experiments studying human arm movements (e.g., Abend *et al.*, 1982; Georgopoulos *et al.*, 1981; Morasso, 1981). This property can be accounted for by various optimization principles evolving through computations acquired through a learning process, such as the minimum jerk principle (Hogan, 1982, 1984; Yashin-Flash, 1983; Flash and Hogan, 1985) or the minimum torque change principle (Uno *et al.*, 1989; Kawato *et al.*, 1990; Osu *et al.*, 1997). However, smooth bell-shaped velocity profiles can also be accounted for by dynamic properties of muscle activation (Partridge, 1966) and dynamic properties of signal transfer within the central nervous system (Partridge, 1973). Instead of modeling complex properties of muscle cells, neurons, and synapses, a simplified model can be used that only retains some basic characteristics of neural signal transmission. This can be accomplished by using a cascade of low-pass filters on the activation level $u(t)$ (Partridge 1966, 1973):

$$\dot{\varphi}_i(t) = \frac{\varphi_{i-1}(t) - \varphi_i(t)}{\tau}, \ 1 \le i \le n, \tag{6}$$

where τ is the time constant of the filter, n denotes the number of filters applied, $\varphi_0(t)$ is the incoming signal, and $\varphi_n(t)$ is the filtered signal. Miller and Sinkjaer (1998) suggest that a second-order low-pass filter with the time constant of 40 ms produces a good fit to the data they acquired.

The spring-mass system with fractional-power damping (5) augmented with the second-order low-pass temporal filter is described by the following equations:

$$\begin{aligned}
&m\ddot{x} + b \cdot \text{sign}(\dot{x}) \cdot |\dot{x}|^{\frac{1}{5}} + k(x-u) = 0, \\
&\dot{\varphi}_i = \frac{\varphi_{i-1} - \varphi_i}{\tau}, \ 1 \le i \le 2, \\
&\varphi_0 = \bar{u}, \\
&u = \varphi_2.
\end{aligned} \tag{7}$$

Here x, $\varphi_0, \ldots, \varphi_2$, $\bar{u}$, and u are functions of time; φ_1, φ_2 denote the state variables of the second-order low-pass filter, $\bar{u}$ denotes the activation function provided by the central nervous system, u denotes the actual effective activation of the muscle pair. The value used for τ was equal to 40 ms. For system (7) the position of the object x, the effective activation u, the primary activation $\bar{u}$, and the temporal filter state variables φ_1, φ_2 are all measured in units of length. It is assumed that prior to each movement the system stays in the initial position $x(0)$ with zero velocity and with the primary activation $\bar{u}$ set to $x(0)$, such that the effective activation u is equal to $x(0)$. Figure 2 shows a typical movement of the spring-mass system with fractional-power damping and filtered activation. The primary activation signal used to produce this movement is the same pulse-step combination as the one used to produce the movement shown in Figure 1.

Fractional-power damping causes a very special behavior of the system at low velocities: a so-called stiction region in the position space. This phenomenon is described in the next section.

4   Stiction region

Figure 4 shows the damping force as a function of the movement velocity for the fractional-power damping model compared to that for the linear damping model. Nonlinear damping of this kind causes a relatively high damping force for lower velocities and relatively low damping for higher velocities. The low damping at high velocities allows for fast movements whereas the high damping for low velocities allows for efficient termination of movements without waiting for oscillations to decay. These features make it possible to accomplish movements faster and to stop in a desired
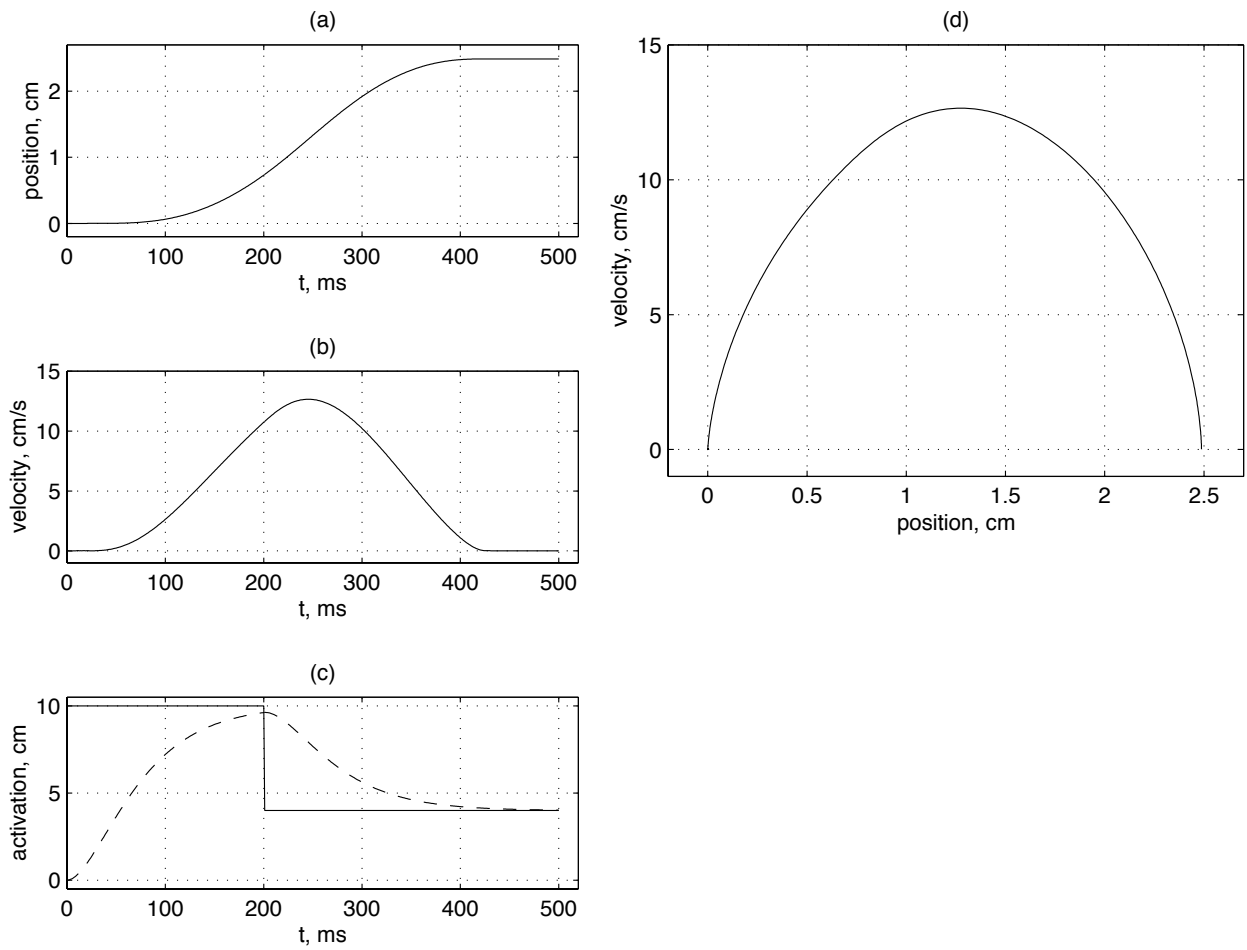
Figure 2: A typical movement of the mass with fractional-power damping and filtered activation. Panels *(a)*, *(b)*, and *(c)* show, respectively, the movement position, velocity, and the control signal as a function of time. The dashed line in panel *(c)* shows the effective activation $u(t)$ obtained from $\bar{u}(t)$ by temporal filtering.
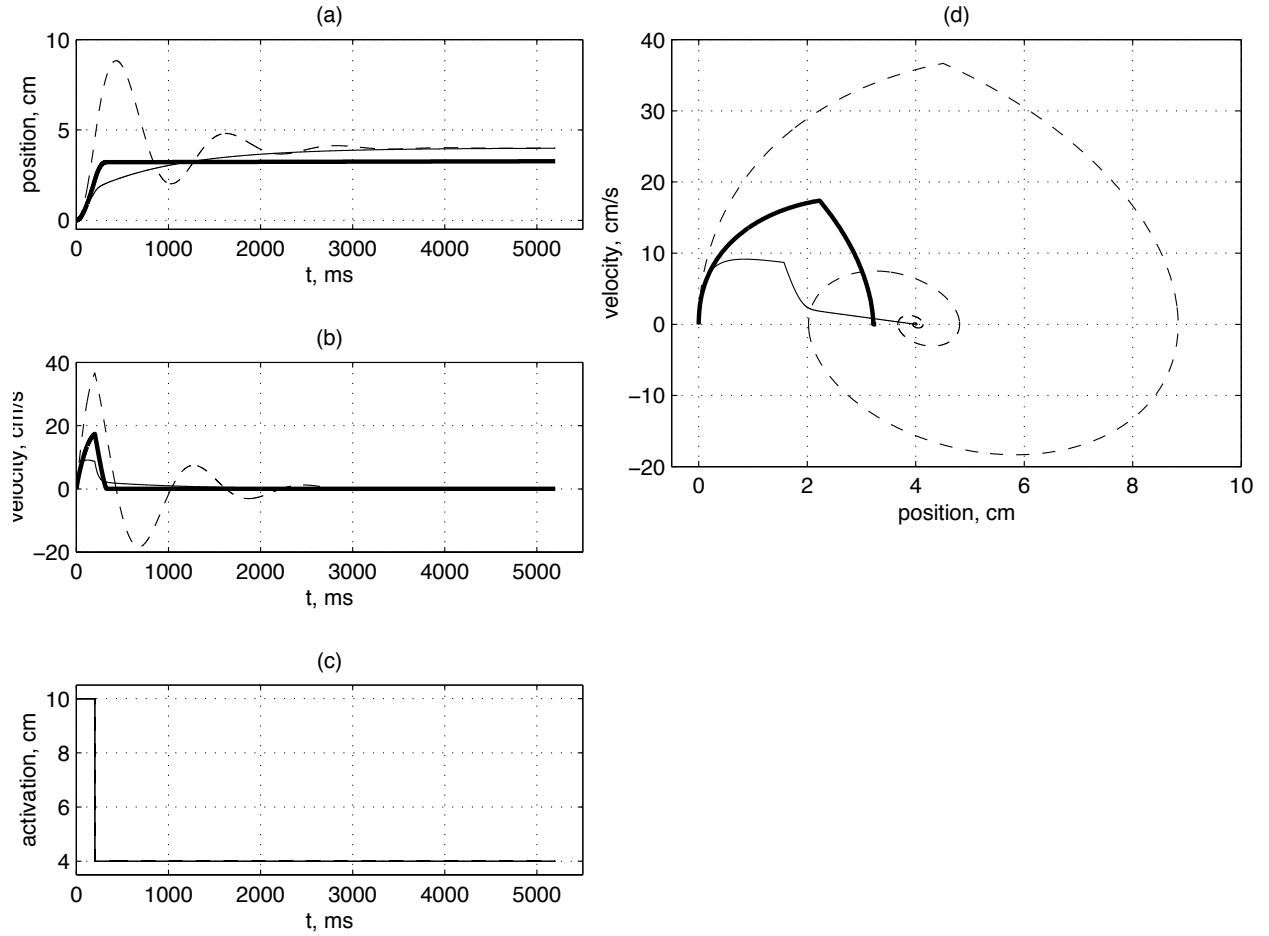
Figure 3: A typical movement of the mass with fractional-power damping compared to a movement of the same system with linear damping. Panels *(a)*, *(b)*, and *(c)* show, respectively, the movement position, velocity, and the control signal as a function of time. Panel *(d)* shows the phase space trajectory of the movement. All the movements are produced by the same pulse-step combination. No temporal filtering is applied. The thick solid lines in panels *(a,b,d)* show the trajectory of the system with fractional-power damping (the damping coefficient $b = 3$ N $\left(\frac{s}{m}\right)^{\frac{1}{5}}$). The dashed lines show the trajectory of the system with linear damping and the damping coefficient $b = 3$ N $\frac{s}{m}$. The thin solid lines show the trajectory of the system with linear damping and ten times higher value for the damping coefficient, $b = 30$ N $\frac{s}{m}$.

location more easily. Figure 3 illustrates this point. It shows a typical movement of the mass-spring system with fractional-power damping compared to the same kind of movement of the system with linear damping. Figure 3 shows two movements of the linear damping system with two different values of the damping coefficient b. A small damping coefficient causes the mass to oscillate for long time about the equilibrium position before it comes to rest. A large damping coefficient causes the entire movement to be very slow. Fractional-power damping enables the combinations of fast movement with efficient stopping without oscillation.
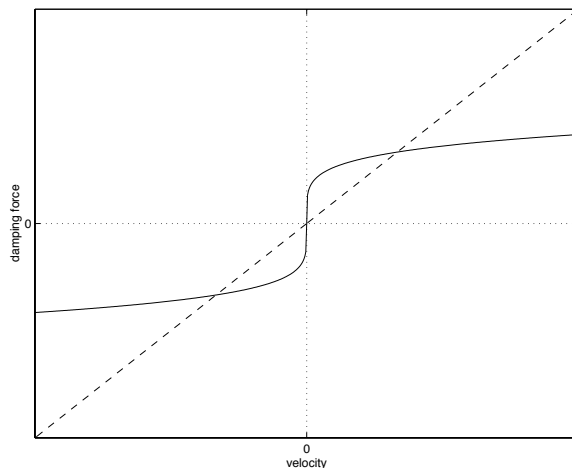

Figure 4: Damping force as a function of movement velocity for the fractional-power damping model (solid line) compared to that for the linear damping model (dashed line).

However, high damping for low velocities causes the mass to effectively stop quite far from the equilibrium position. The mass does not stop completely, but its velocity drops very close to zero and remains there. It would take an extremely long time to reach the equilibrium position from such a state, an infinite time for all practical purposes. Thus, such a state can be considered a stable state of the system for practical purposes. This kind of stable states appear around the true equilibrium state. The region around the equilibrium position consisting of such pseudo-stable states is called the stiction region. The activation level u determines the true equilibrium position and hence the location of the stiction region as well.

In our simulations we used precomputed stiction region borders as a function of the activation level u. These data are shown in Figure 5. The procedure used to compute the stiction region borders is described in Appendix.

5 Experiments description

In our experiments the pulse-step control scheme was used (Robinson, 1975; Ghez, 1979; Ghez and Martin, 1982; Gottlieb, 1993). Figure 6 shows a pulse-step control signal as a function of time and specifies the notation. The control signal is a piecewise constant function of time consisting of two phases, the pulse phase and the step phase. The activation level $u(t)$ (or the primary activation $\bar{u}(t)$ in cases when the temporal filtering is applied, see Section 3) is set to a constant magnitude
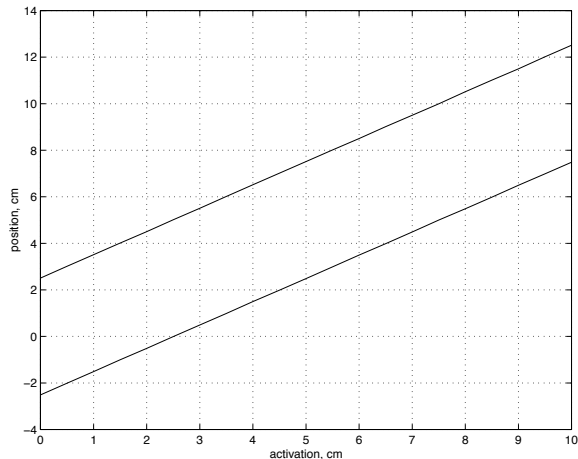
Figure 5: The stiction region borders as a function of the activation level.

u_p for time d_p, and then is switched to another magnitude u_s. The term pulse magnitude will be used for the pulse activation level u_p, the term pulse duration will be used for the switch time d_p, and the term step magnitude will be used for the step activation level u_s.
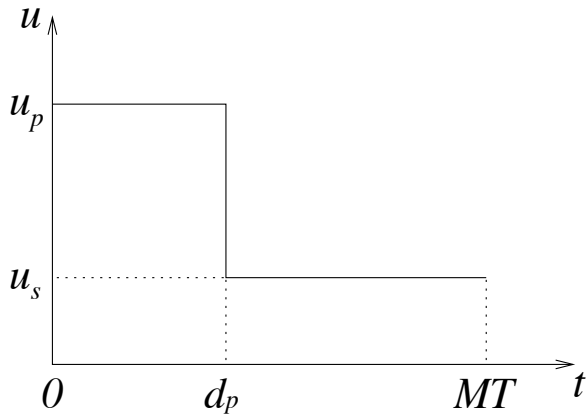

Figure 6: Pulse-step control notation. The control signal is a piecewise constant function of time consisting of two steps or phases, the pulse phase and the step phase. The pulse magnitude is denoted by u_p, the pulse duration is denoted by d_p, the step magnitude is denoted by u_s, and the total movement duration is denoted by MT.

The step phase of the movement does not have a preset duration. In these experiments no corrective signals or any kind of learning took place; a pulse-step combination determined by the pulse magnitude, pulse duration, and step magnitude is sent over to the system in a purely feed forward manner. A movement is judged complete when the plant enters the stiction region of the state space for activation u_s (see equations (13), (14)). Let us denote the total movement duration by MT (see Figure 6). Thus, the pulse-step control combination and the entire movement are defined by a set of three parameters, u_p, u_s, and d_p. Figures 1 and 2 show samples of such

10

movements. The position of the system when a movement is complete is called the final position of the movement.

The purpose of the experiments was to assess the final position variability for series of similar movements with noisy control signal or plant dynamics. The final position spread is different for movements of different amplitudes, velocities, and durations. To produce different movements we used pulse-step combinations with different pulse magnitudes with the same pulse duration and the same step magnitude. For each particular pulse magnitude we simulated a large number of movements while various parameters of the control signal or the state of the plant were perturbed. We perturbed a chosen parameter one at a time while all other parameters remained fixed for the particular set of movements. The perturbations were normally distributed with zero mean. The existing literature suggests many various mechanisms causing noise in the control signal or in the plant dynamics. We have studied several noise injection models:

1. Stochastic pulse magnitude, u_p.

2. Stochastic pulse duration, d_p.

3. Stochastic plant dynamics.

Details of the stochastic plant dynamics simulation are described in Section 6.3.

In all these noise injection schemes the variance of the final position arises due to the presence of the stiction region. For a similar system with linear damping there is one stable point for each activation level, so the final position is completely determined by the step magnitude and no final position variance can appear under the present paradigm.

For the system with fractional-power damping the step magnitude determines location of the stiction region. Each movement necessarily terminates within the stiction region, but since the stiction region spans quite large area in the position space, different movements can terminate in different position within the stiction region. Thus final position of each movement does not depend solely on the step magnitude but on other parameters of the control signal as well. It also depends on the initial position of the movement; in these experiments we used the same initial position for all movements and analyzed the movement amplitude among other parameters. The main point of this research is to investigate how the final position variance depends on pulse magnitude as well as average velocity, amplitude, and duration of the movement.

6 Experimental results

We used the pulse-step combinations with pulse duration $d_p = 200$ ms, step magnitude $u_s = 5$ cm, and pulse magnitude u_p assuming values between 8 cm and 20 cm. These pulse-step combinations were used as the nominal control signal which underwent various disturbances. The pulse-step combinations and the corresponding movements are shown in Figures 7 and 8. Figure 7 shows the movements for the system with no temporal filtering, Figure 8 shows the movements for the system with temporal filtering. The stiction region for this particular step magnitude u_s span positions from 2.49 cm to 7.52 cm. For all movements simulated in our experiments the initial position $x(0)$ was equal to zero, the initial velocity $\dot{x}(0)$ was equal to zero as well.

Let a series of movements be a set of simulated movements using the same pulse magnitude or the same mean pulse magnitude. Each data point in any of the plots below represents a series of movements. In all the experiments the number of movements in one series is equal to 10,000.
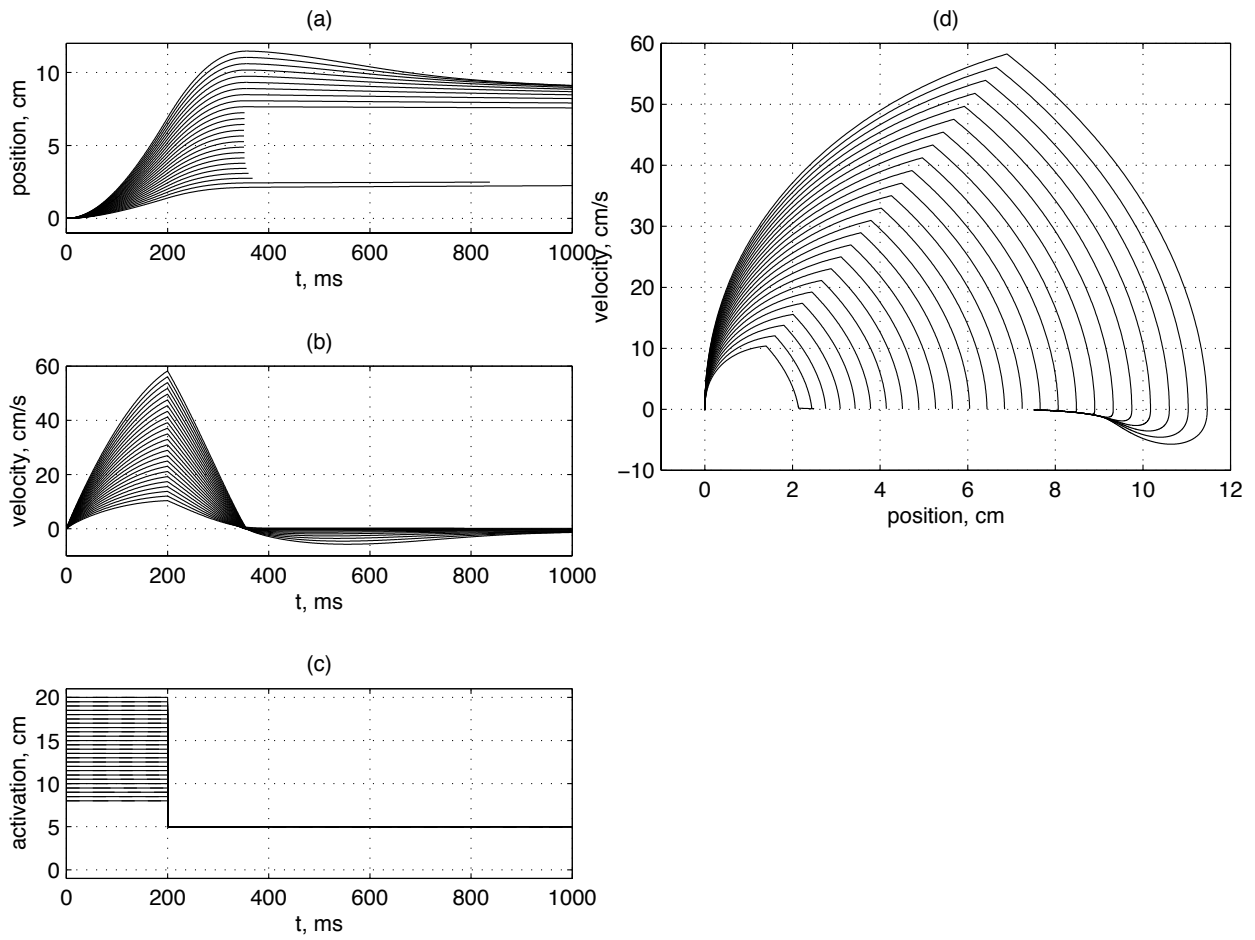
Figure 7: Movements of the system with no temporal filtering for various pulse magnitudes without any disturbances. The pulse magnitude assumes values between 8 cm and 20 cm. Panels *(a)*, *(b)*, and *(c)* show, respectively, the movement position, velocity, and the control signal as a function of time. Panel *(d)* shows the phase space trajectories of the movements.
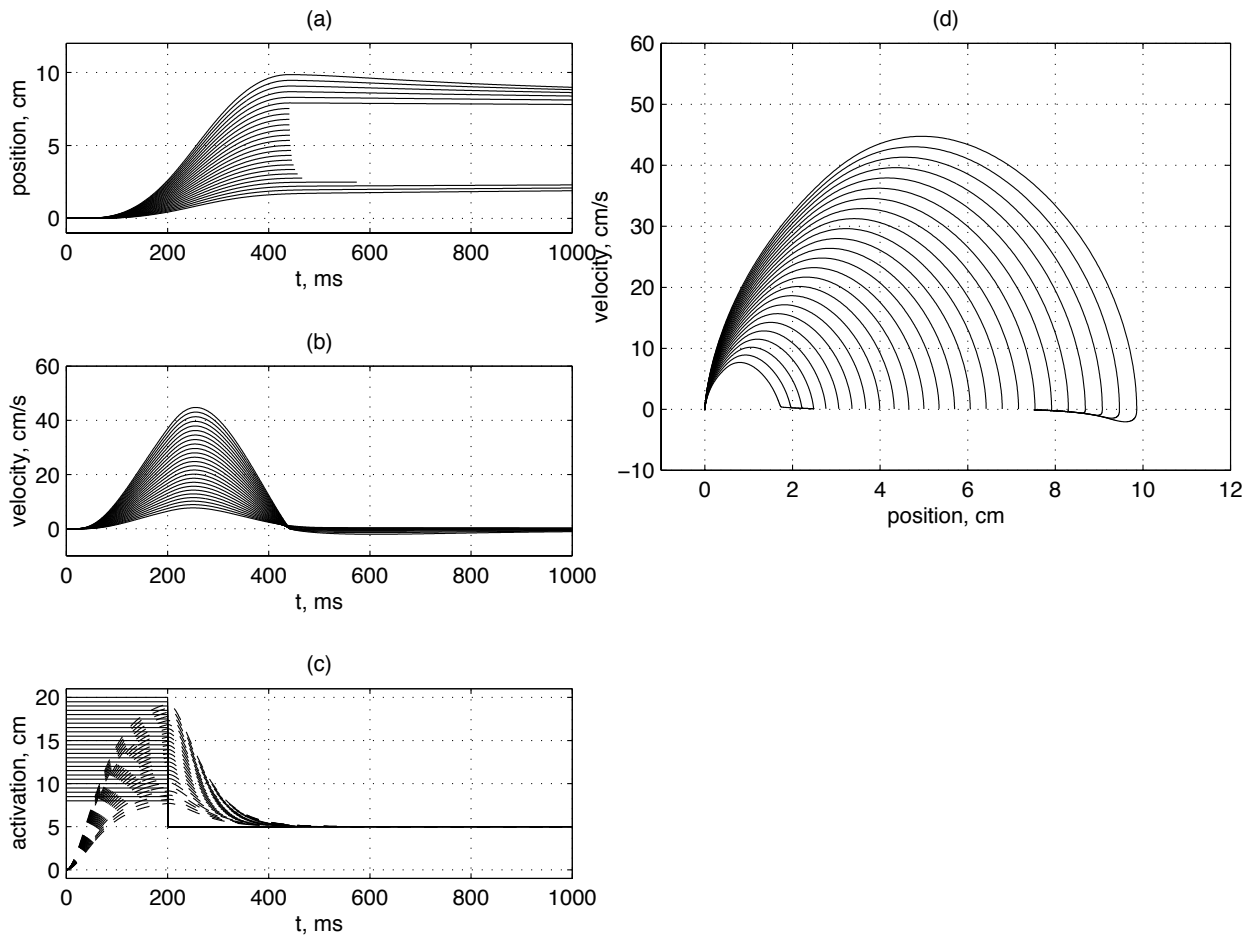
Figure 8: Movements of the system with temporal filtering for various pulse magnitudes without any disturbances. The pulse magnitude assumes values between 8 cm and 20 cm. Panels *(a)*, *(b)*, and *(c)* show, respectively, the movement position, velocity, and the control signal as a function of time. Panel *(d)* shows the phase space trajectories of the movements.

The most critical characteristic of a series of movements is whether all the movements from the series terminate in the inner area of the stiction region, or some of them terminate at one of the edges of the stiction region. Since we consider a system with a single degree of freedom, the stiction region has two edges which are points on the position axis. Let us call the edge which is closer to the initial position the proximal edge, and the edge which is far from the initial position the distal edge. Let us call the movements ending up in the inner area of the stiction region internal movements, and the movements ending up at one of the edges — proximal edge movements or distal edge movements. If some movements in a movement series are proximal edge movements this entire series is called a proximal edge series. Similarly, if some movements in a movement series are distal edge movements this entire series is called a distal edge series. If all movements in a movement series are internal movements this series is called an internal series.

Below we present the results of the experiments with various noise injection models. In all the experiments the simulation time-step dt is equal to 1 ms.

6.1   Stochastic pulse magnitude

In this set of experiments each series of movements includes pulse-step combinations with different pulse magnitudes u_p, but the mean pulse magnitude $\mu(u_p)$ is fixed for each series. Different series though use different mean pulse magnitude. The mean pulse magnitude values were equally spaced every 0.5 cm between 8 cm and 16 cm, so there are total of 17 series. All the pulse-step combinations had the same step magnitude $u_s = 5$ cm, and the same pulse-duration $d_p = 200$ ms. The pulse magnitude was perturbed by Gaussian noise with standard deviation equal to 0.4 cm. This injected noise produces final position spreads that are neither too small nor too large relative to the size of the stiction region, thus making it possible to observe changes in the final position variance for various mean pulse magnitudes.

Figure 9 shows the standard deviation of the final position for different mean pulse magnitudes and the data for classification of the movement series as proximal edge series, internal series, and distal edge series. Panels *(a)*, *(b)*, and *(c)* show the data for the system with no temporal filtering, panels *(d)*, *(e)*, and *(f)* show the data for the system with temporal filtering.

Panels *(a)* and *(d)* in Figure 9 show the final position standard deviation $\sigma(x_f)$ as a function of the mean pulse magnitude. The data points corresponding to proximal edge series are shown by squares, points corresponding to internal series are shown by circles, and points corresponding to distal edge series are shown by triangles. The same convention is used in all the plots throughout this section.

As one can see in panels *(a)* and *(d)* in Figure 9 the data from proximal edge series make a good linear fit as well as the data from internal series and the data from distal series. Each of the three sets of data though makes a fit which is substantially different from the two others. The lines in panels *(a)* and *(d)* in Figure 9 show the three linear fits, the corresponding covariance coefficients are shown in Table 1.

The sharp decrease of standard deviations as the mean pulse magnitude decreases for proximal series is due to the increase in the proportion of proximal edge movements in each new series. Figure 10 shows several representative movements for one of the proximal series for the system with no temporal filtering. Figure 11 shows several representative movements for one of the proximal series for the system with temporal filtering. Analogously the sharp decrease of standard deviations as the mean pulse magnitude increases for distal series is due to the increase in the proportion of
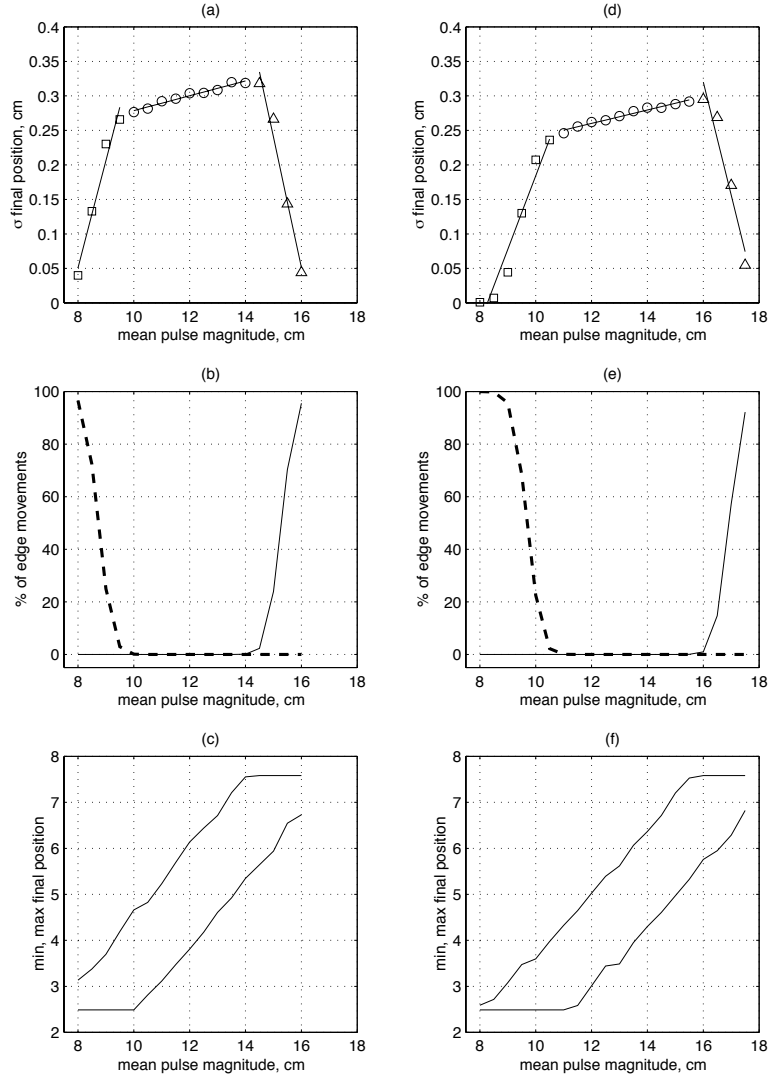
Figure 9: *(a,b,c)*. Data for the system with no temporal filtering. *(d,e,f)*. Data for the system with temporal filtering. *(a,d)*. The standard deviation of final positions as a function of the mean pulse magnitude. The data points corresponding to proximal series are shown by squares, points corresponding to internal series are shown by circles, and points corresponding to distal edge series are shown by triangles. The covariance coefficients for the linear fits are shown in Table 1. *(b,e)*. The fraction of proximal edge movements and the fraction of distal edge movements in different series as a function of the mean pulse magnitude. The dashed line shows the fraction of proximal edge movements, the solid line shows the fraction of distal edge movements. *(c,f)*. The minimal final position and maximal final position in different series as a function of the mean pulse magnitude.

fig	x-axis	y-axis	TF	linear fit parameters		
				proximal	internal	distal
9(a)	$\mu\left(u_p\right)$	$\sigma\left(x_f\right)$	x	$r^2 = 0.97$	$r^2 = 0.96$	$r^2 = 0.98$
(b)	$\mu\left(u_p\right)$	% of edge movements	x			
(c)	$\mu\left(u_p\right)$	$\min\left(x_f\right), \max\left(x_f\right)$	x			
(d)	$\mu\left(u_p\right)$	$\sigma\left(x_f\right)$	v	$r^2 = 0.95$	$r^2 = 0.97$	$r^2 = 0.94$
(e)	$\mu\left(u_p\right)$	% of edge movements	v			
(f)	$\mu\left(u_p\right)$	$\min\left(x_f\right), \max\left(x_f\right)$	v			
16(a)	$\mu\left(u_p\right)$	V	x	$r^2 = 0.99$	$r^2 = 1.00$	$r^2 = 0.94$
(b)	V	$\sigma\left(x_f\right)$	x	$r^2 = 0.99$ $\beta_0 = 0.00$ cm	$r^2 = 0.96$ $\beta_0 = 0.23$ cm	$r^2 = 0.99$ $\beta_0 = -0.03$ cm
(c)	$\log_2\left(\frac{2A}{\sigma}\right)$	MT	x	$r^2 = 0.99$	$r^2 = 0.63$	$r^2 = 1.00$
(d)	$\mu\left(u_p\right)$	V	v	$r^2 = 0.95$	$r^2 = 1.00$	$r^2 = 0.88$
(e)	V	$\sigma\left(x_f\right)$	v	$r^2 = 1.00$ $\beta_0 = -0.02$ cm	$r^2 = 0.97$ $\beta_0 = 0.21$ cm	$r^2 = 0.99$ $\beta_0 = -0.05$ cm
(f)	$\log_2\left(\frac{2A}{\sigma}\right)$	MT	v	$r^2 = 0.95$	$r^2 = 0.87$	$r^2 = 1.00$
17(a)	$\log_2\left(\frac{2A}{\sigma}\right)$	MT	x		$r^2 = 0.63$	
(b)	$\log_2\left(\frac{2A}{\sigma}\right)$	MT	v		$r^2 = 0.87$	
18(a)	V	$\frac{A}{MT}$	x	$r^2 = 0.93$ $\beta_0 = -1.38$ cm/s $\beta_1 = 1.05$	$r^2 = 1.00$ $\beta_0 = -0.01$ cm/s $\beta_1 = 1.00$	$r^2 = 0.84$ $\beta_0 = -3.12$ cm/s $\beta_1 = 0.95$
(b)	V	$\frac{A}{MT}$	v	$r^2 = 0.95$ $\beta_0 = -0.32$ cm/s $\beta_1 = 0.95$	$r^2 = 1.00$ $\beta_0 = -0.01$ cm/s $\beta_1 = 1.00$	$r^2 = 0.87$ $\beta_0 = -3.62$ cm/s $\beta_1 = 1.09$

Table 1: Summarized description of what is shown in data figures in Section 6.1 and the numerical data for all the linear fits shown in those figures. Field **TF** specifies whether the temporal filtering was applied. Notation β_0, β_1 is used to denote respectively the intercepts and slopes of the linear fits. See text for further explanations.

distal edge movements in each new series. Figure 12 shows several representative movements for one of the distal series for the system with no temporal filtering. Figure 13 shows several representative movements for one of the distal series for the system with temporal filtering.
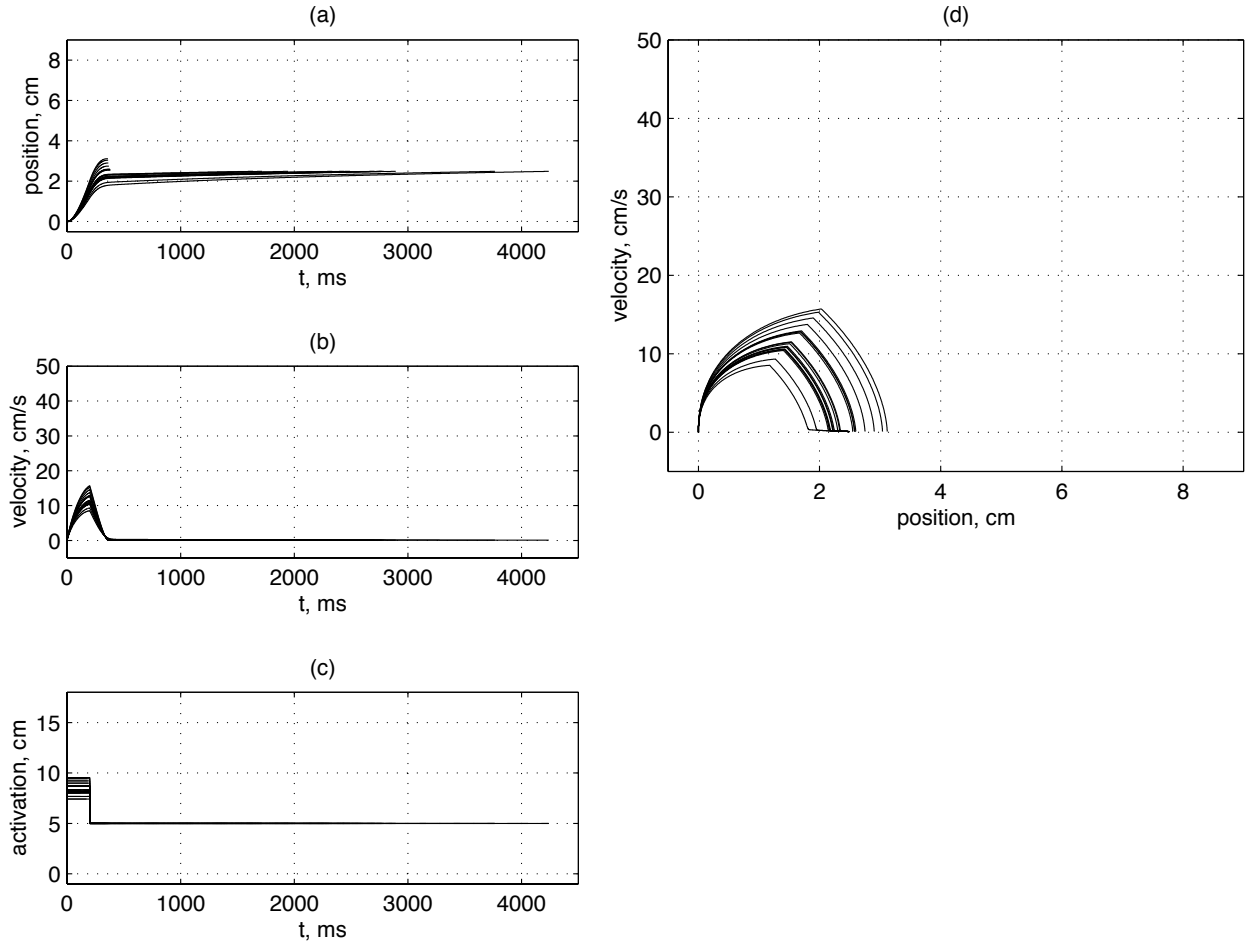

Figure 10: Representative proximal edge movements with stochastic pulse magnitude, system with no temporal filtering. Mean pulse magnitude is equal to 8.5 cm. Panels *(a)*, *(b)*, and *(c)* show, respectively, the movement position, velocity, and the control signal as a function of time. Panel *(d)* shows the phase space trajectories of the movements.

Figure 14 shows several representative movements for one of the internal series for the system with no temporal filtering. In each of the internal series, all the movements terminate in the inner area of the stiction region neither undershooting nor overshooting it. Figure 15 shows several representative movements for one of the internal series for the system with temporal filtering.

Panels *(b)* and *(e)* in Figure 9 show the fraction of proximal edge movements and the fraction of distal edge movements in different series versus the corresponding mean pulse magnitude. The dashed line shows the fraction of proximal edge movements, the solid line shows the fraction of distal edge movements. These data provide the criterion used to classify the series as proximal, internal, or distal.
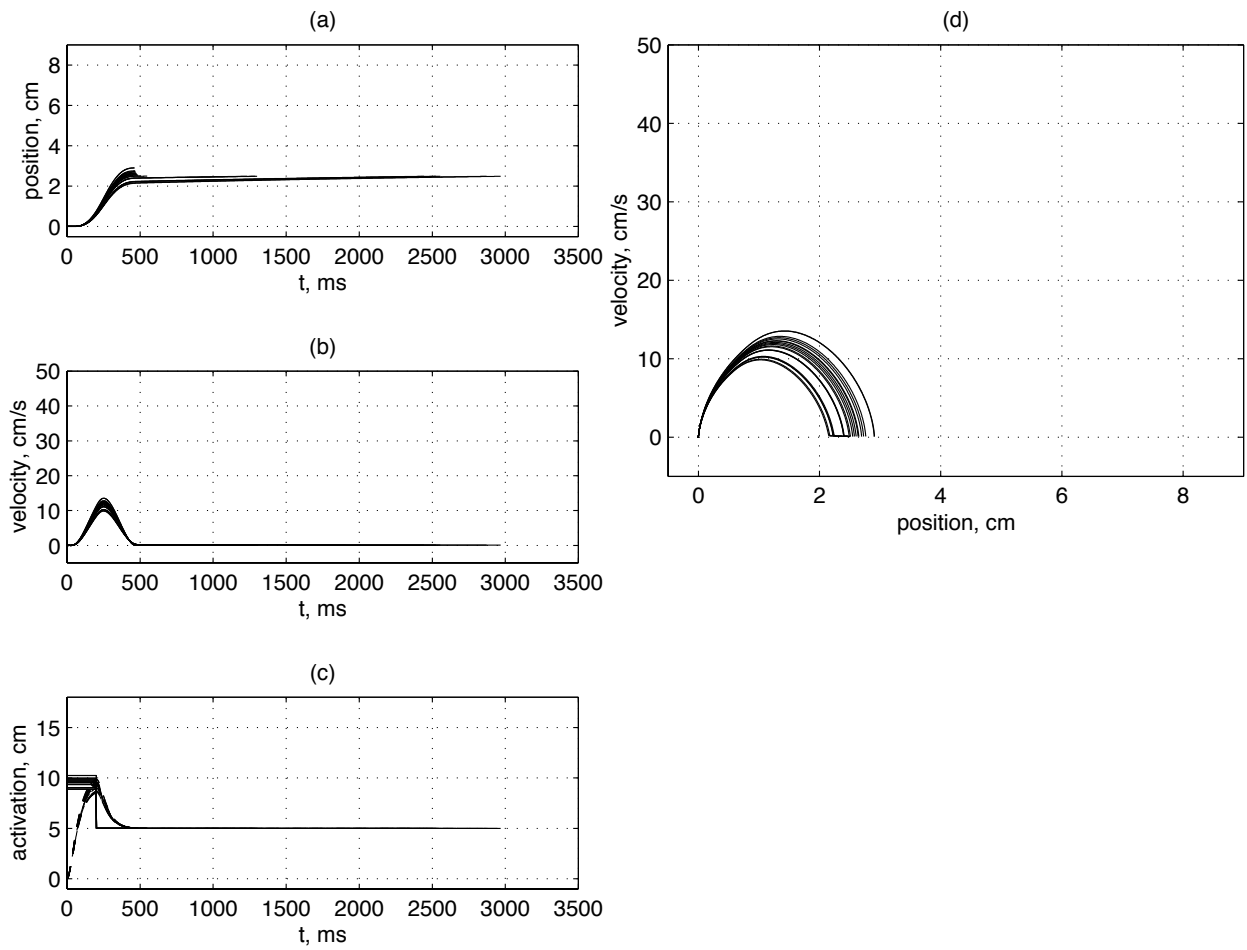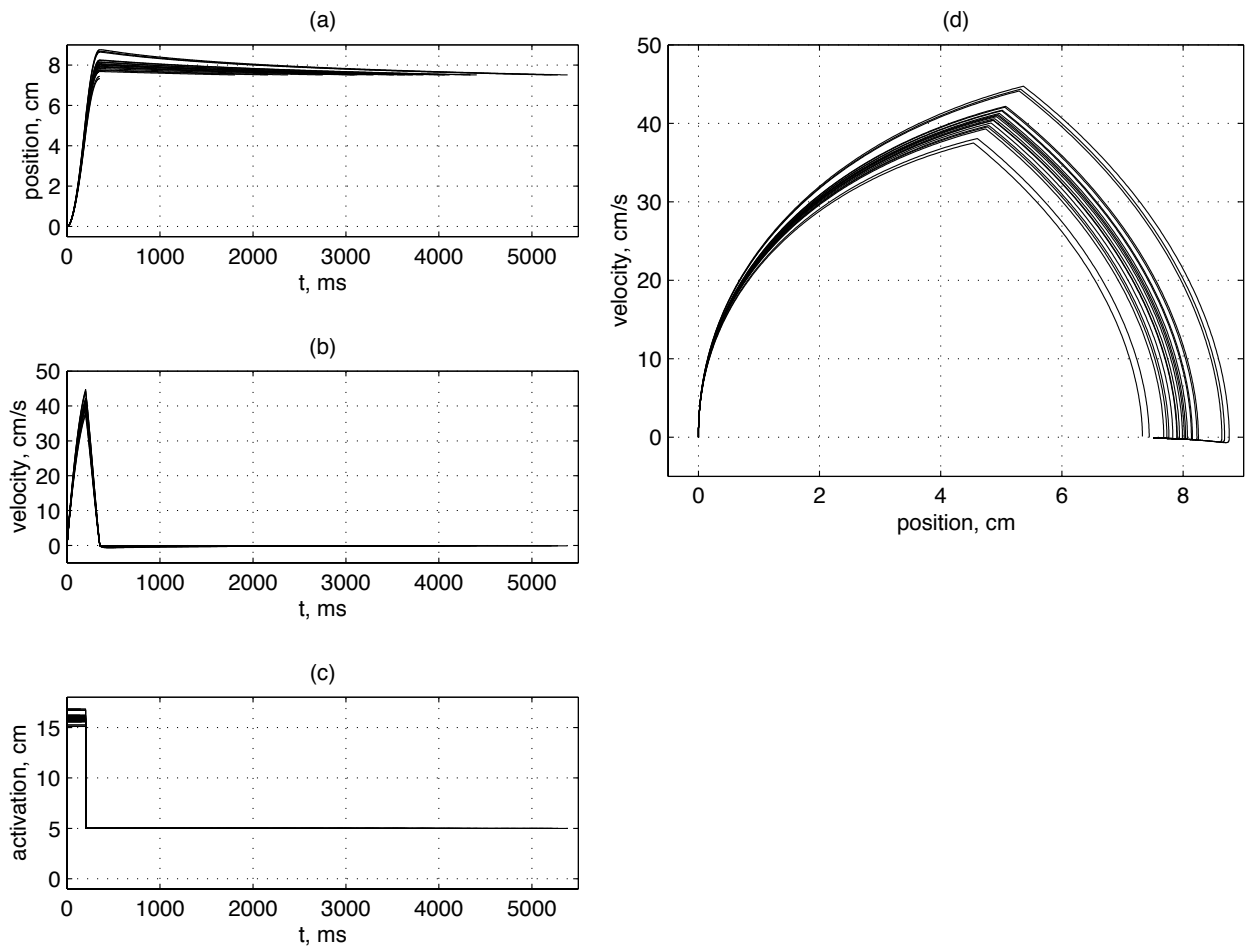
17

Figure 11: Representative proximal edge movements with stochastic pulse magnitude, system with temporal filtering. Mean pulse magnitude is equal to 9.5 cm. Panels *(a)*, *(b)*, and *(c)* show, respectively, the movement position, velocity, and the control signal as a function of time. Panel *(d)* shows the phase space trajectories of the movements.
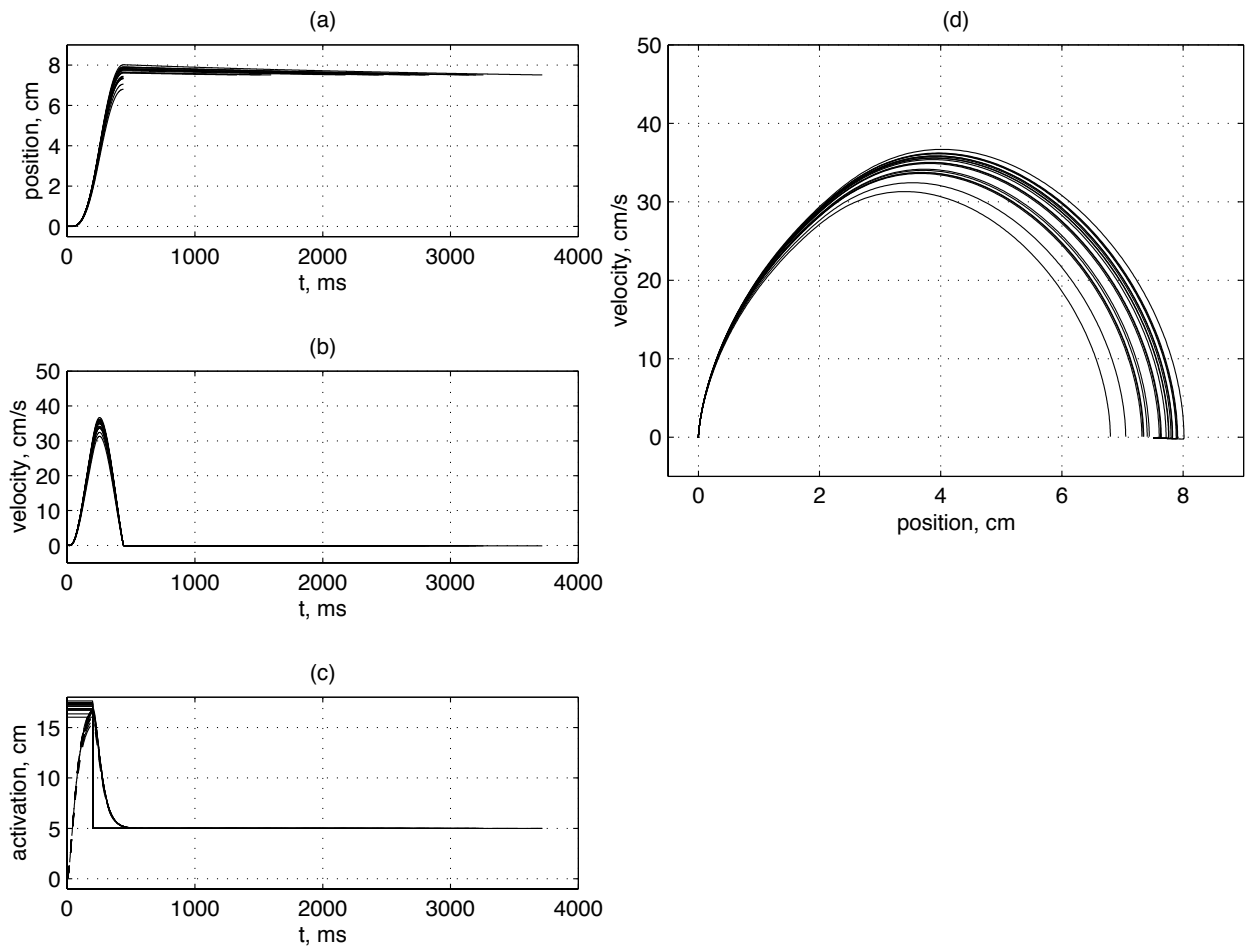
Figure 12: Representative distal edge movements with stochastic pulse magnitude, system with no temporal filtering. Mean pulse magnitude is equal to 16 cm. Panels *(a)*, *(b)*, and *(c)* show, respectively, the movement position, velocity, and the control signal as a function of time. Panel *(d)* shows the phase space trajectories of the movements.
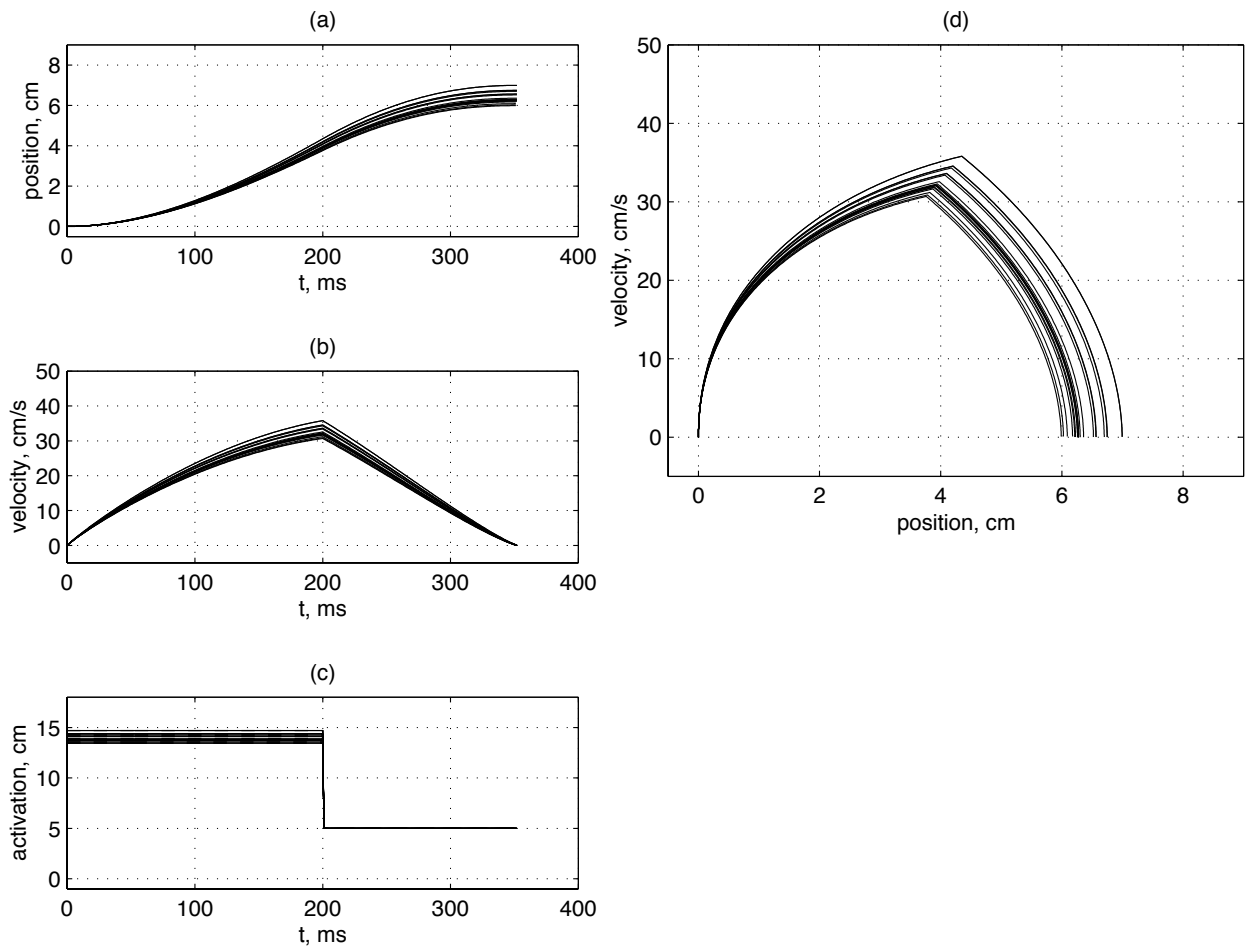
Figure 13: Representative distal edge movements with stochastic pulse magnitude, system with temporal filtering. Mean pulse magnitude is equal to 17 cm. Panels *(a)*, *(b)*, and *(c)* show, respectively, the movement position, velocity, and the control signal as a function of time. Panel *(d)* shows the phase space trajectories of the movements.

Figure 14: Representative internal movements with stochastic pulse magnitude, system with no temporal filtering. Mean pulse magnitude is equal to 14 cm. Panels *(a)*, *(b)*, and *(c)* show, respectively, the movement position, velocity, and the control signal as a function of time. Panel *(d)* shows the phase space trajectories of the movements.
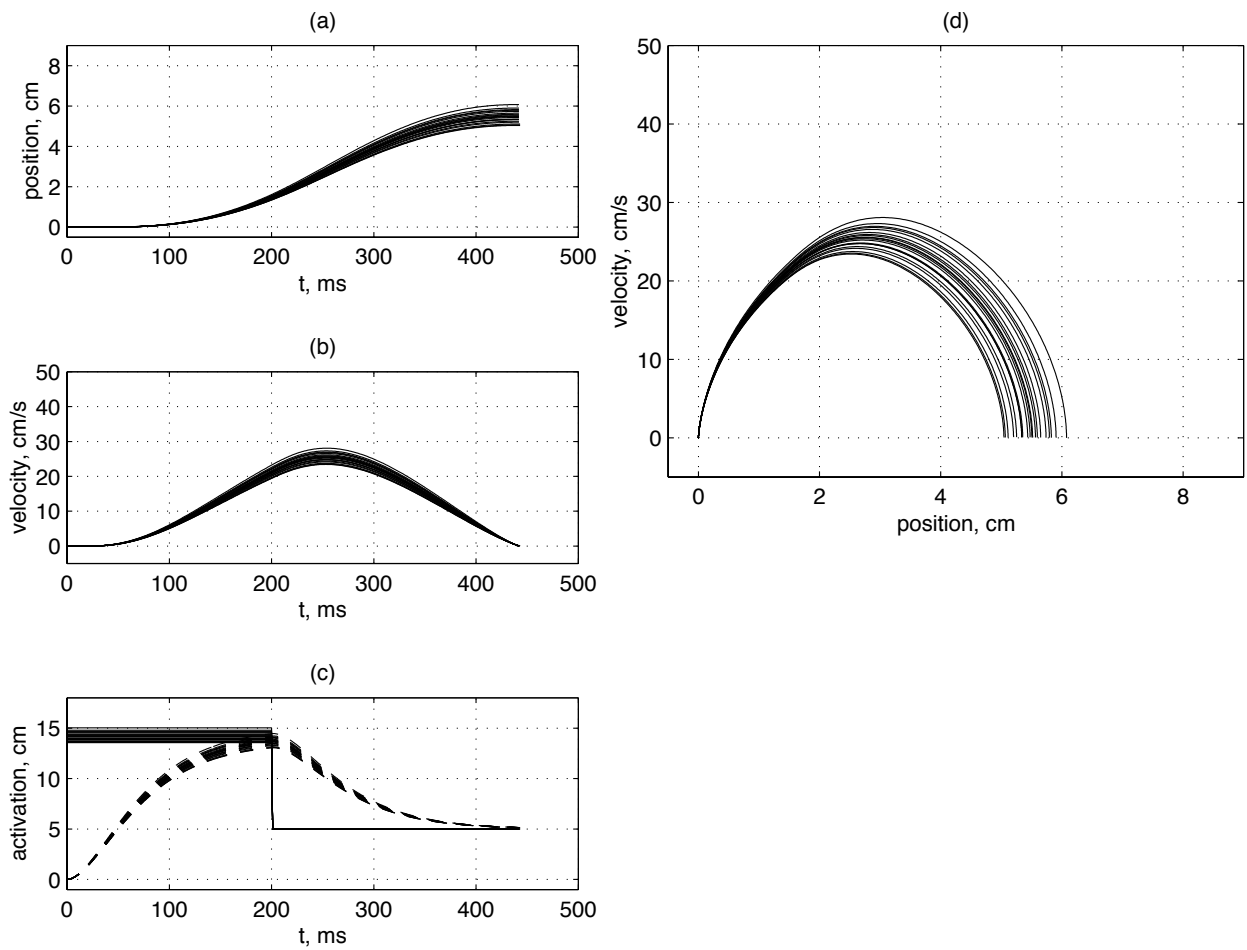
Figure 15: Representative internal movements with stochastic pulse magnitude, system with temporal filtering. Mean pulse magnitude is equal to 14 cm. Panels *(a)*, *(b)*, and *(c)* show, respectively, the movement position, velocity, and the control signal as a function of time. Panel *(d)* shows the phase space trajectories of the movements.

Panels *(c)* and *(f)* in Figure 9 show the minimal final position and maximal final position in different series versus the corresponding mean pulse magnitude. These data help to gain more insights on how the final positions are distributed for different mean pulse magnitudes and how the final position locations relate to the stiction region location. The constant part of the minimal final position line at the proximal series area corresponds to the proximal edge of the stiction region. Analogously the constant part of the maximal final position line at the distal series area corresponds to the distal edge of the stiction region.

Table 1 provides a summarized description of what is shown in every panel of Figure 9 and in other figures of this section. It also provides the numerical data for all the linear fits shown in the figures.

Figure 16 shows how the average velocity of the movements relates to the standard deviation of final positions and to the mean pulse magnitude. It also shows the same data plotted in terms of equation (2) (see Section 2) which is the generic formulation of Fitts' law. Panels *(a)*, *(b)*, and *(c)* show the data for the system with no temporal filtering. Panels *(d)*, *(e)*, and *(f)* show the data for the system with temporal filtering.

Panels *(a)* and *(d)* in Figure 16 show the average velocity as a function of the mean pulse magnitude. Here the average velocity is computed separately for each movement:

$$V = \frac{1}{n} \sum_{i=1}^{n} \frac{A_i}{MT_i}. \tag{8}$$

Here V stands for the average velocity for certain series of movements, A_i is the amplitude of i-th movement, MT_i is the movement time, n is the number of movements in the series, $n = 10,000$ for all series. Similar to the data shown in panels *(a)* and *(d)* in Figure 9 the data from proximal edge series, internal series, and distal series make three separate good linear fits. The corresponding covariance coefficients are shown in Table 1.

All the works providing evidence for a linear speed-accuracy relationship (Schmidt *et al.*, 1979; Wright and Meyer, 1983; etc.) analyze the data in terms of equation (3) (see Section 2), i.e. the standard deviation of the final positions or the effective target width as a function of the average velocity. Panels *(b)* and *(e)* in Figure 16 show these data. In this representation, as well as in the ones described earlier, the data from proximal series, internal series, and distal series make three separate good linear fits. Another salient feature of these data is that for proximal and distal fits the intercepts are very close to zero. For all practical purposes, the intercepts are equal to zero. The corresponding covariance coefficients and the intercepts are shown in Table 1.

Panels *(c)* and *(f)* in Figure 16 show the average movement time as a function of the index of difficulty (Fitts, 1954):

$$ID = \log_2 \left(\frac{2A}{\sigma(x_f)} \right).$$

Here A is the average movement amplitude for a series of movements:

$$A = \frac{1}{n} \sum_{i=1}^{n} A_i, \tag{9}$$

where A_i is the amplitude of i-th movement. The notation $\sigma(x_f)$ stands for the standard deviation of final positions for a series of movements. It corresponds to the effective target width W in (2)
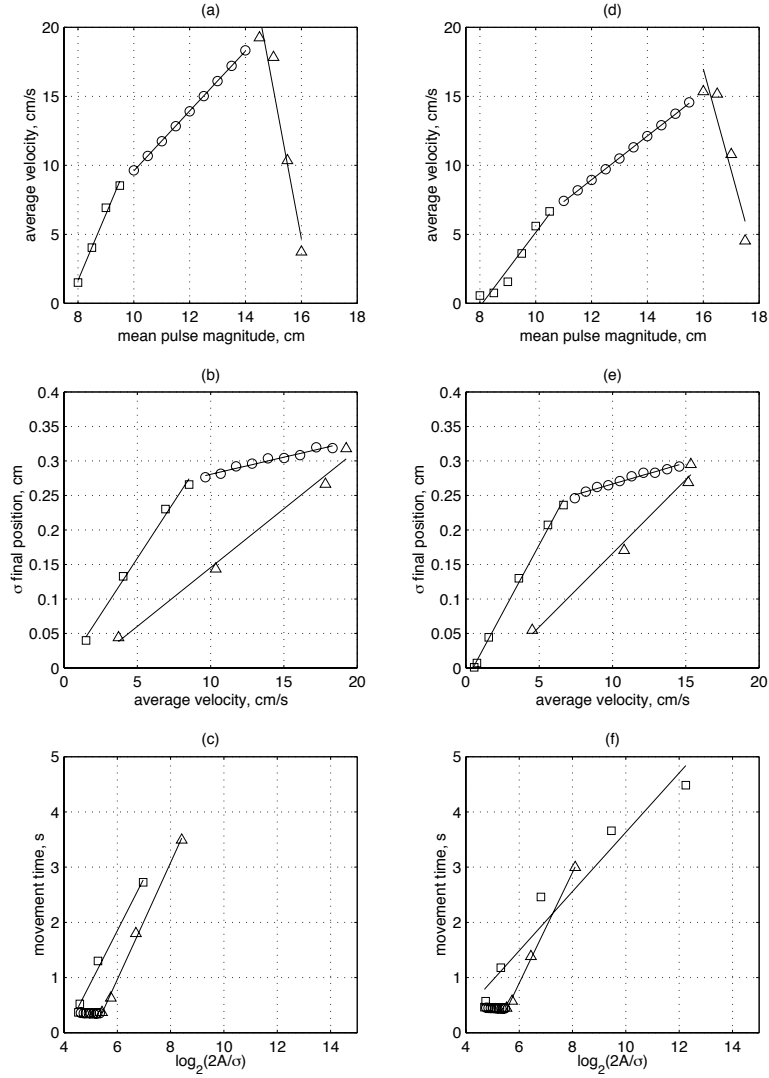
Figure 16: The relationship of the average velocity to the standard deviation of final positions and to the mean pulse magnitude. *(a,b,c)*. Data for the system with no temporal filtering. *(d,e,f)*. Data for the system with temporal filtering. *(a,d)*. The average velocity as a function of the mean pulse magnitude. *(b,e)*. The standard deviation of the final positions as a function of the average velocity. *(c,f)*. The average movement time as a function of the index of difficulty. The data points corresponding to proximal series are shown by squares, points corresponding to internal series are shown by circles, and points corresponding to distal edge series are shown by triangles. The covariance coefficients and intercepts for the linear fits are shown in Table 1.

24

and in the relevant literature. The movement time for a series here is computed by averaging durations of movements of the series:

$$MT = \frac{1}{n} \sum_{i=1}^{n} MT_i. \tag{10}$$

The proximal series and the distal series make two separate good linear fits. The internal series do not make a good linear fit although the differences between average movement times of internal series are very small compared to those for proximal series or for distal series. Figure 17 shows the same data for the internal series in a finer scale. The covariance coefficients for all Fitts' law linear fits are shown in Table 1.
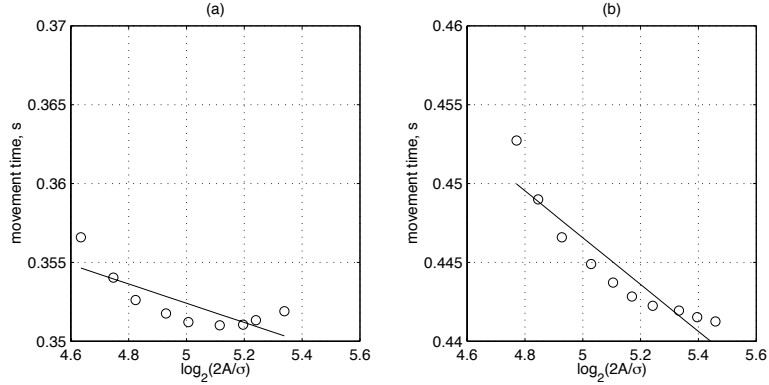

Figure 17: The average movement time as a function of the index of difficulty for internal series of movements. *(a)*. Data for the system with no temporal filtering. *(b)*. Data for the system with temporal filtering. The covariance coefficients for the linear fits are shown in Table 1.

Here we face an obvious contradiction. The same data make a good fit with both linear and logarithmic dependence. To clarify this, let us rewrite (3) so that it is formulated in the same terms as (2):

$$W = c + d \cdot \frac{A}{MT}$$

yields

$$MT = d \cdot \frac{A}{W - c}. \tag{11}$$

We have shown (see Figure 16*(b,e)* and Table 1) that the intercepts c for proximal and distal series are equal to zero for practical purposes. Then (11) becomes

$$MT = d \cdot \frac{A}{W},$$

or, writing $\sigma(x_f)$ instead of W and assuming another value for the fit parameter d,

$$MT = d \cdot \frac{2A}{\sigma(x_f)},$$

which is different from the fit shown in panels 16*(c,f)*:

$$MT = a + b \cdot \log_2 \left(\frac{2A}{\sigma \left(x_f \right)} \right).$$

One of the possible explanations of this contradiction is that the average velocity V computed as in (8) is not necessary equal to the average movement amplitude A divided by the average movement time MT calculated as in (9) and (10) respectively:

$$\exists \{A_i\}, \{MT_i\} : \quad \frac{\sum_{i=1}^n A_i}{\sum_{i=1}^n MT_i} \neq \frac{1}{n} \sum_{i=1}^n \frac{A_i}{MT_i}.$$

We checked whether these two ways to compute average velocity produce the same results for our data. Figure 18 shows the average amplitude (9) divided by the average movement time (10) versus the average velocity (8). For the internal series this relationship is the identical one for all practical purposes, while for the proximal and distal series this relationship is substantially nonlinear. The corresponding covariance coefficients, the slope, and intercept values are shown in Table 1.
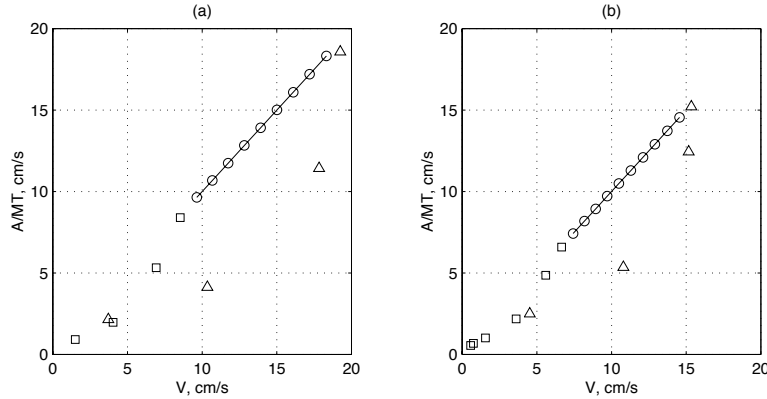

Figure 18: The average amplitude (equation (9)) divided by the average movement time (equation (10)) versus the average velocity (equation (8)). *(a)*. Data for the system with no temporal filtering. *(b)*. Data for the system with temporal filtering. The data points corresponding to proximal series are shown by squares, points corresponding to internal series are shown by circles, and points corresponding to distal edge series are shown by triangles. The covariance coefficients, intercepts, and slopes for the linear fits are shown in Table 1.

6.2   Stochastic pulse duration

In this set of experiments each series of movements includes pulse-step combinations with different pulse duration magnitudes d_p. Different series use different pulse magnitude values. The pulse magnitude values were equally spaced every 0.5 cm between 8 cm and 16 cm, so there is a total of 17 series. All the pulse-step combinations had the same step magnitude $u_s = 5$ cm, and the same mean pulse-duration $\mu \left(d_p \right) = 200$ ms. The pulse duration was perturbed by Gaussian noise with standard deviation equal to 20 ms. This injected noise produces final position spreads that are

neither too small, nor too large relative to the size of the stiction region, thus making it possible to observe changes in the final position variance for various pulse magnitudes.

Figure 19 shows the standard deviation of the final position for different pulse magnitudes and the data for classification of the movement series as proximal edge series, internal series, and distal edge series. Panels *(a)*, *(b)*, and *(c)* show the data for the system with no temporal filtering. Panels *(d)*, *(e)*, and *(f)* show the data for the system with temporal filtering.

Panels *(a)* and *(d)* in Figure 19 show the final position standard deviation $\sigma(x_f)$ as a function of the pulse magnitude. As in the previous section, the data points corresponding to proximal edge series are shown by squares, points corresponding to internal series are shown by circles, and points corresponding to distal edge series are shown by triangles.

As one can see in panels *(a)* and *(d)* in Figure 19, the data from internal series make a good linear fit, as well as the data from proximal edge series. The data from distal series do not make a good linear fit but they clearly obey a pattern which is quite different from the other two kinds of data. Each of the three sets of data makes a fit which is substantially different from the two others. The lines in panels *(a)* and *(d)* in Figure 19 show the three linear fits, the corresponding covariance coefficients are shown in Table 2.

fig	x-axis	y-axis	TF	linear fit parameters		
				proximal	internal	distal
19*(a)*	u_p	$\sigma(x_f)$	x	$r^2 = 0.99$	$r^2 = 1.00$	$r^2 = 0.95$
(b)	u_p	% of edge movements	x			
(c)	u_p	$\min(x_f), \max(x_f)$	x			
(d)	u_p	$\sigma(x_f)$	v	$r^2 = 0.96$	$r^2 = 1.00$	$r^2 = 0.96$
(e)	u_p	% of edge movements	v			
(f)	u_p	$\min(x_f), \max(x_f)$	v			
26*(a)*	u_p	V	x	$r^2 = 0.98$	$r^2 = 1.00$	$r^2 = 0.95$
(b)	V	$\sigma(x_f)$	x	$r^2 = 1.00$ $\beta_0 = -0.03$ cm	$r^2 = 1.00$ $\beta_0 = -0.04$ cm	$r^2 = 1.00$ $\beta_0 = 0.07$ cm
(c)	$\log_2\left(\frac{2A}{\sigma}\right)$	MT	x	$r^2 = 0.99$	$r^2 = 0.10$	$r^2 = 1.00$
(d)	u_p	V	v	$r^2 = 0.96$	$r^2 = 1.00$	$r^2 = 0.96$
(e)	V	$\sigma(x_f)$	v	$r^2 = 1.00$ $\beta_0 = -0.04$ cm	$r^2 = 1.00$ $\beta_0 = 0$ cm	$r^2 = 1.00$ $\beta_0 = 0.07$ cm
(f)	$\log_2\left(\frac{2A}{\sigma}\right)$	MT	v	$r^2 = 1.00$	$r^2 = 0.02$	$r^2 = 1.00$
27*(a)*	$\log_2\left(\frac{2A}{\sigma}\right)$	MT	x		$r^2 = 0.10$	
(b)	$\log_2\left(\frac{2A}{\sigma}\right)$	MT	v		$r^2 = 0.02$	
28*(a)*	V	$\frac{A}{MT}$	x	$r^2 = 0.95$ $\beta_0 = -0.83$ cm/s $\beta_1 = 0.99$	$r^2 = 1.00$ $\beta_0 = 0.14$ cm/s $\beta_1 = 0.99$	$r^2 = 0.78$ $\beta_0 = -0.34$ cm/s $\beta_1 = 1.10$
(b)	V	$\frac{A}{MT}$	v	$r^2 = 0.97$ $\beta_0 = -0.46$ cm/s $\beta_1 = 1.15$	$r^2 = 0.99$ $\beta_0 = 0.77$ cm/s $\beta_1 = 0.93$	$r^2 = 0.83$ $\beta_0 = -0.80$ cm/s $\beta_1 = 1.16$

Table 2: Summarized description of what is shown in data figures in Section 6.2 and the numerical data for all the linear fits shown in those figures. Field **TF** specifies whether the temporal filtering was applied. Notation β_0, β_1 is used to denote respectively the intercepts and slopes of the linear fits. See text for further explanations.

The sharp decrease of standard deviations as the pulse magnitude decreases for proximal series
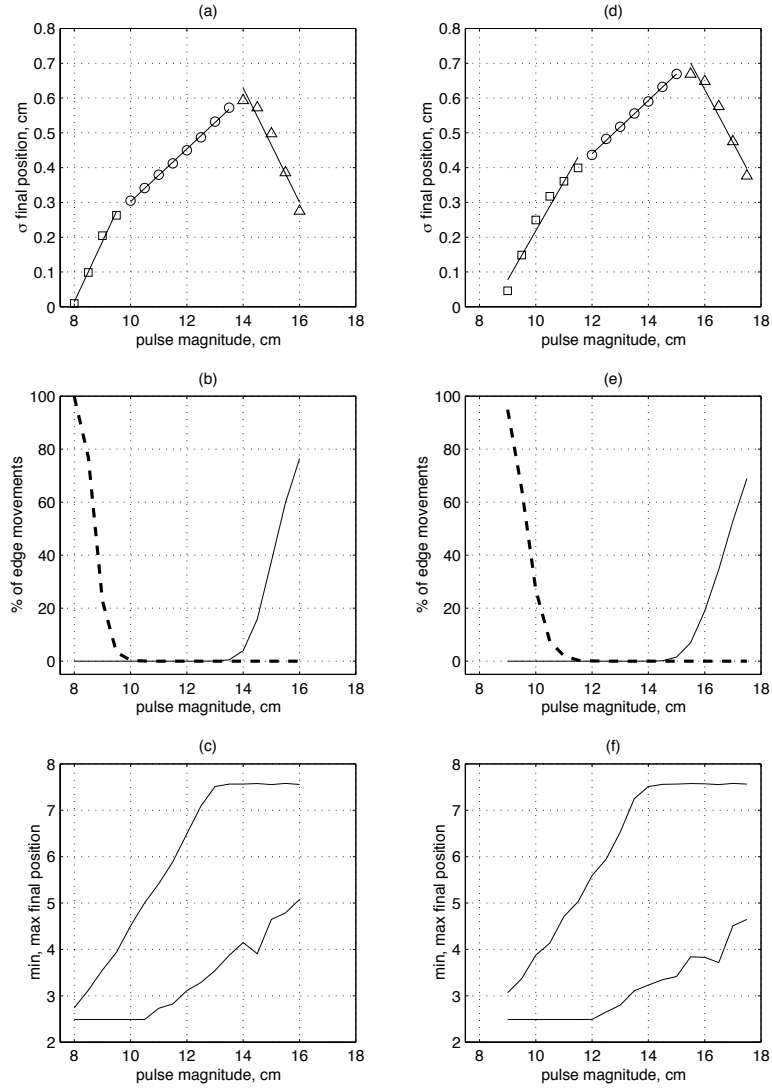
Figure 19: *(a,b,c)*. Data for the system with no temporal filtering. *(d,e,f)*. Data for the system with temporal filtering. *(a,d)*. The standard deviation of final positions as a function of the pulse magnitude. The data points corresponding to proximal series are shown by squares, points corresponding to internal series are shown by circles, and points corresponding to distal edge series are shown by triangles. The covariance coefficients for the linear fits are shown in Table 2. *(b,e)*. The fraction of proximal edge movements and the fraction of distal edge movements in different series as a function of the mean pulse magnitude. The dashed line shows the fraction of proximal edge movements, the solid line shows the fraction of distal edge movements. *(c,f)*. The minimal final position and maximal final position in different series as a function of the pulse magnitude.

28

is due to the increase in the proportion of proximal edge movements in each new series. Figure 20 shows several representative movements for one of the proximal series for the system with no temporal filtering. Figure 21 shows several representative movements for one of the proximal series for the system with temporal filtering. Analogously, the sharp decrease of standard deviations as the pulse magnitude increases for distal series is due to the increase in the proportion of distal edge movements in each new series. Figure 22 shows several representative movements for one of the distal series for the system with no temporal filtering. Figure 23 shows several representative movements for one of the distal series for the system with temporal filtering.
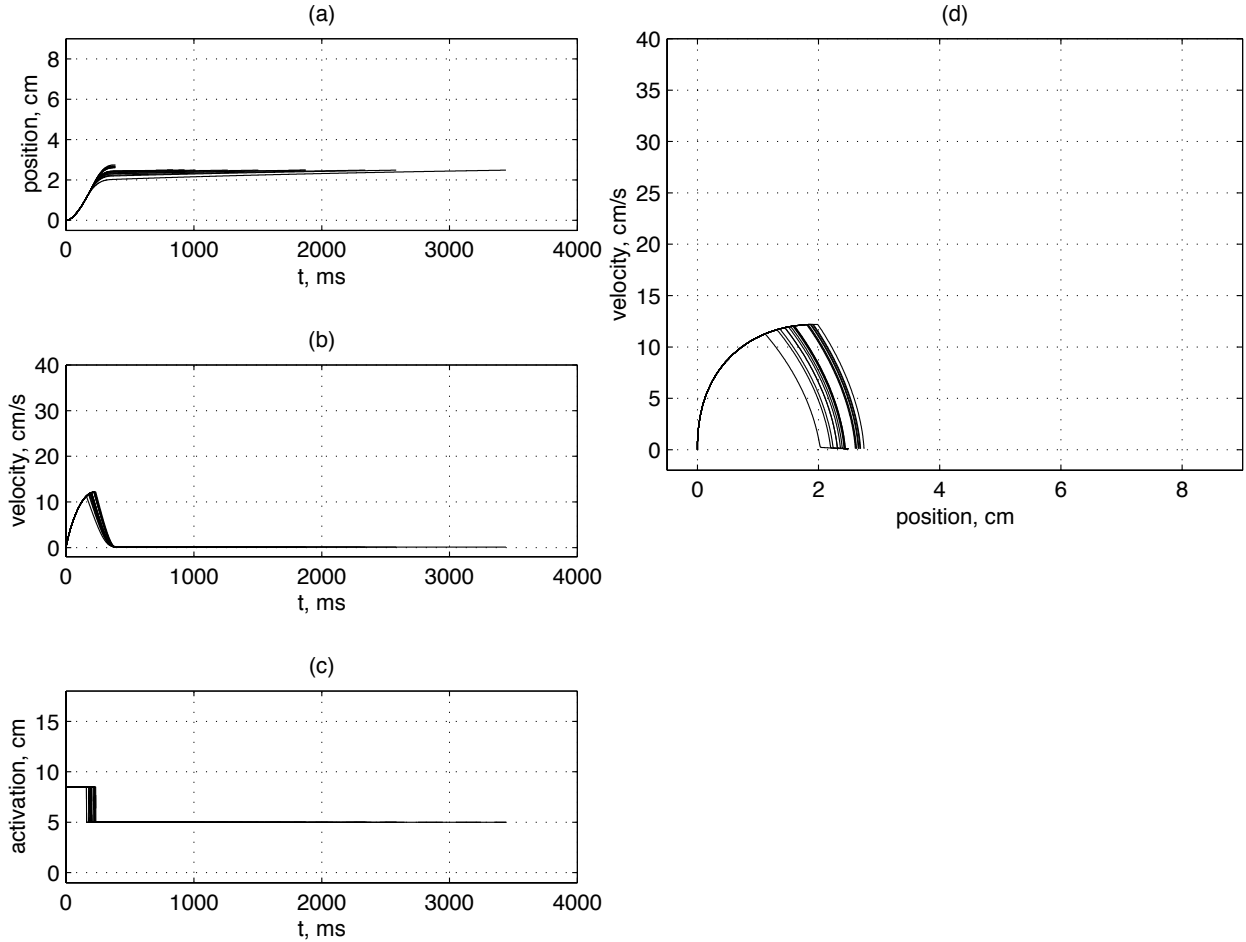

Figure 20: Representative proximal edge movements with stochastic pulse duration, system with no temporal filtering. Pulse magnitude is equal to 8.5 cm. Panels *(a)*, *(b)*, and *(c)* show, respectively, the movement position, velocity, and the control signal as a function of time. Panel *(d)* shows the phase space trajectories of the movements.

Figure 24 shows several representative movements for one of the internal series for the system with no temporal filtering. In each of the internal series all the movements terminate in the inner area of the stiction region, neither undershooting or overshooting it. Figure 25 shows several representative movements for one of the internal series for the system with temporal filtering.
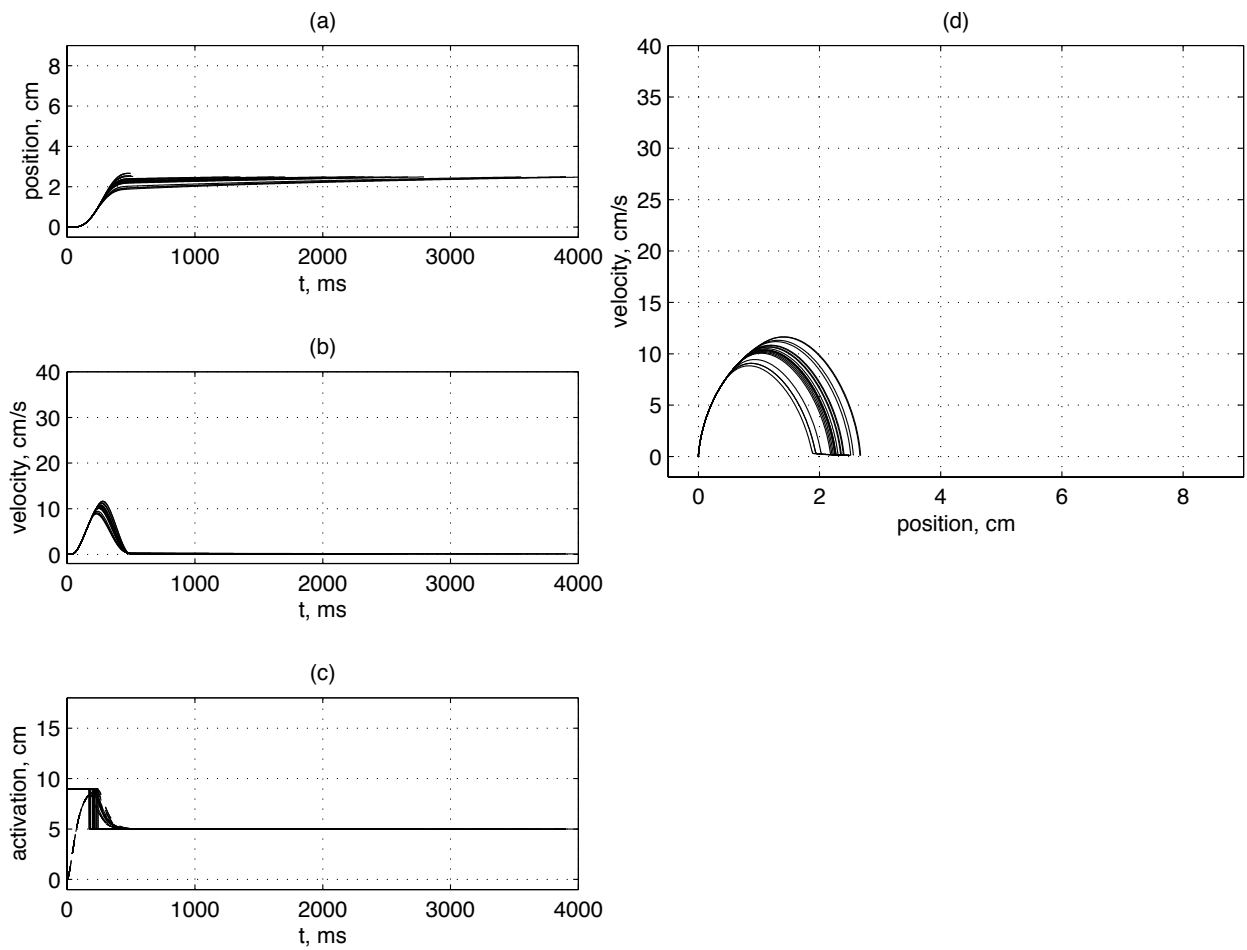
Figure 21: Representative proximal edge movements with stochastic pulse magnitude, system with temporal filtering. Mean pulse magnitude is equal to 9 cm. Panels *(a)*, *(b)*, and *(c)* show, respectively, the movement position, velocity, and the control signal as a function of time. Panel *(d)* shows the phase space trajectories of the movements.
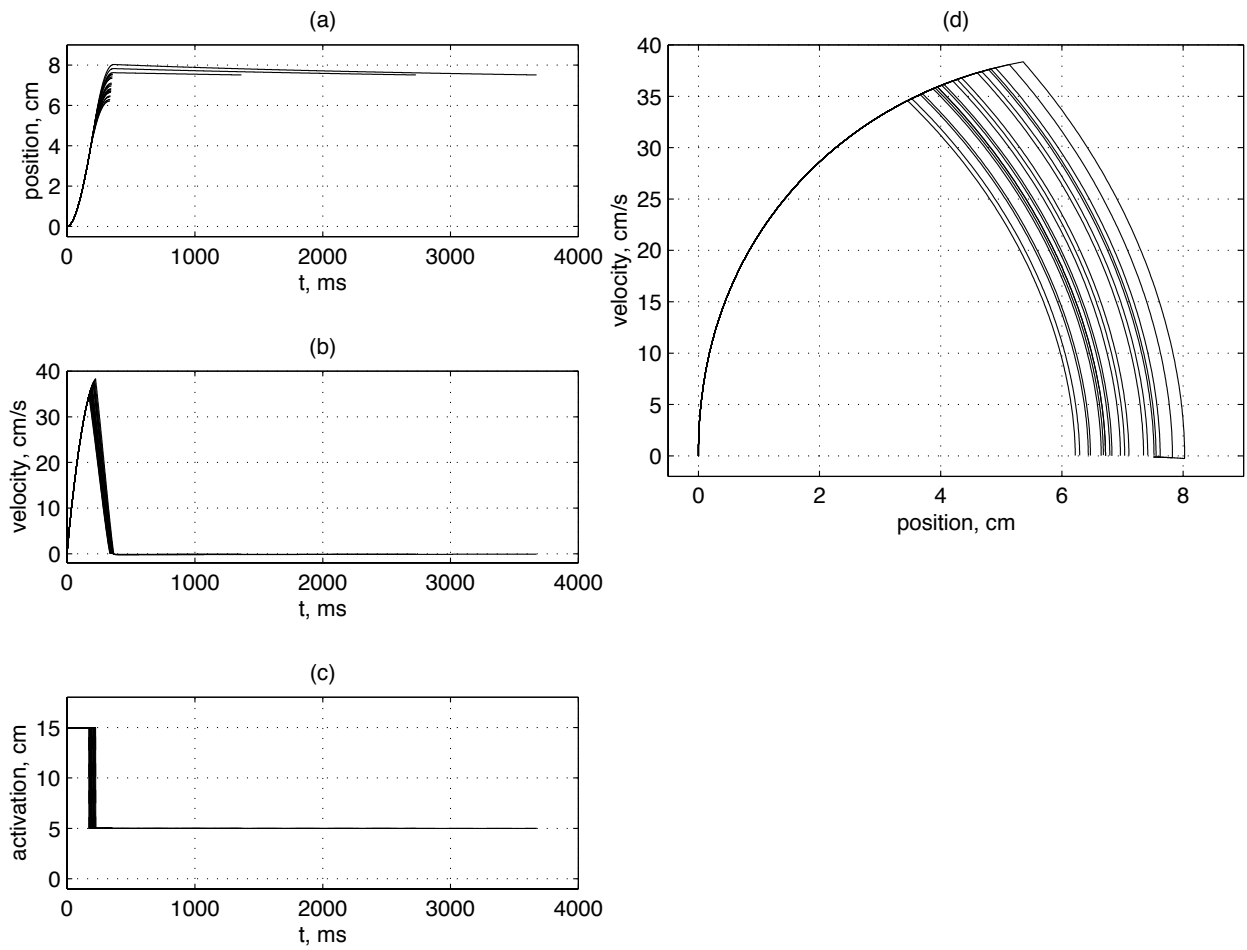
30

Figure 22: Representative distal edge movements with stochastic pulse magnitude, system with no temporal filtering. Mean pulse magnitude is equal to 15 cm. Panels *(a)*, *(b)*, and *(c)* show, respectively, the movement position, velocity, and the control signal as a function of time. Panel *(d)* shows the phase space trajectories of the movements.
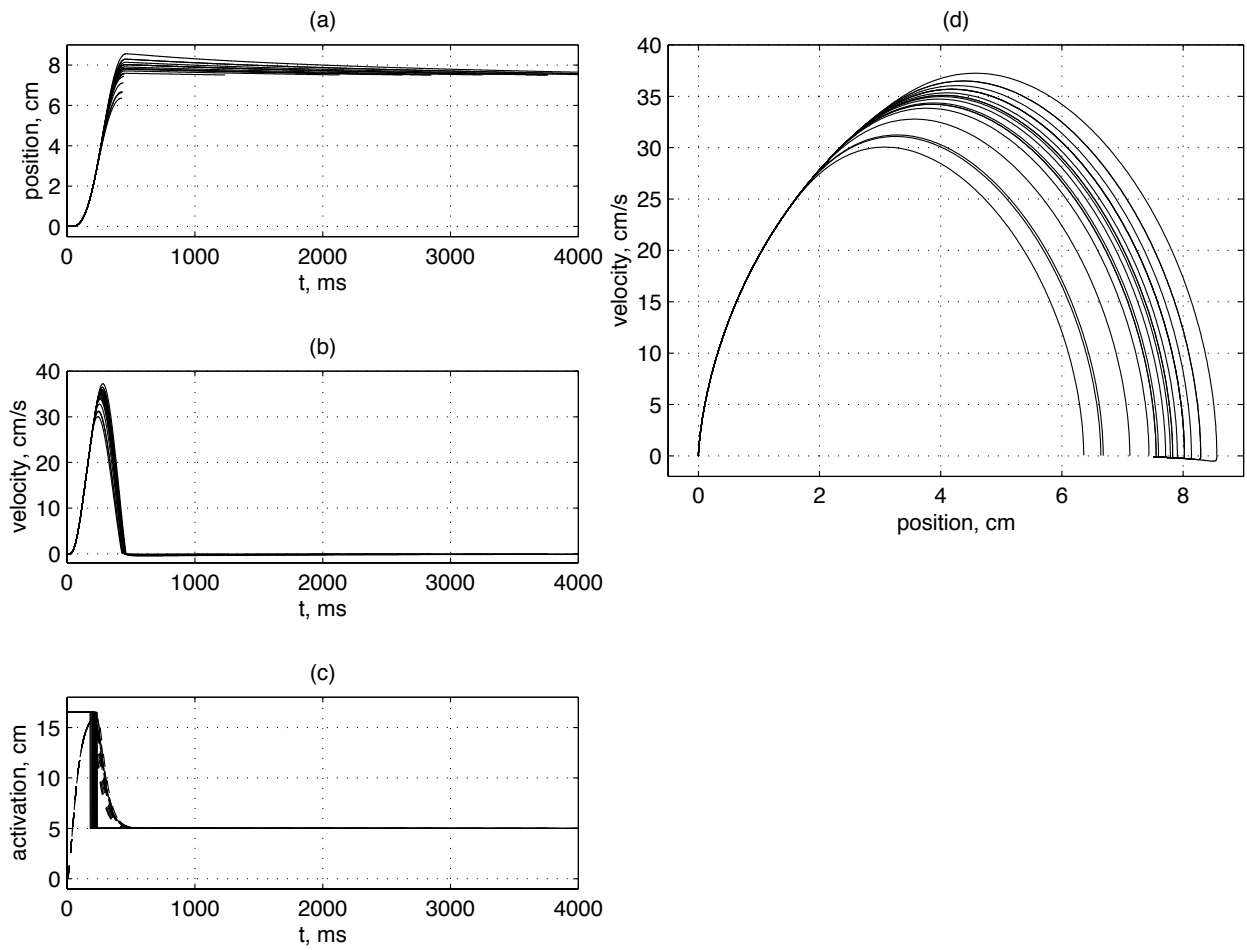
Figure 23: Representative distal edge movements with stochastic pulse magnitude, system with temporal filtering. Mean pulse magnitude is equal to 16.5 cm. Panels *(a)*, *(b)*, and *(c)* show, respectively, the movement position, velocity, and the control signal as a function of time. Panel *(d)* shows the phase space trajectories of the movements.
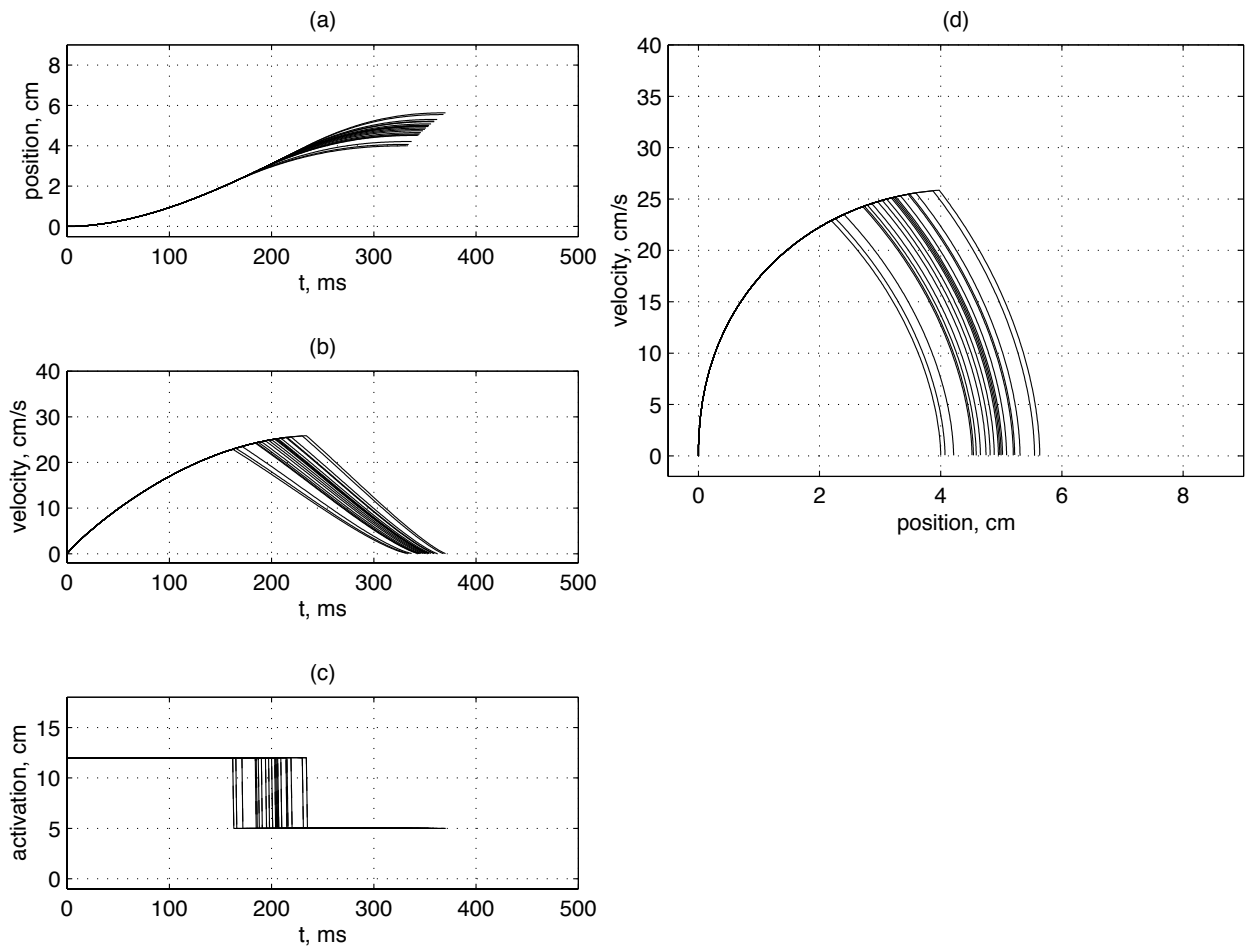
Figure 24: Representative internal movements with stochastic pulse magnitude, system with no temporal filtering. Mean pulse magnitude is equal to 12 cm. Panels *(a)*, *(b)*, and *(c)* show, respectively, the movement position, velocity, and the control signal as a function of time. Panel *(d)* shows the phase space trajectories of the movements.
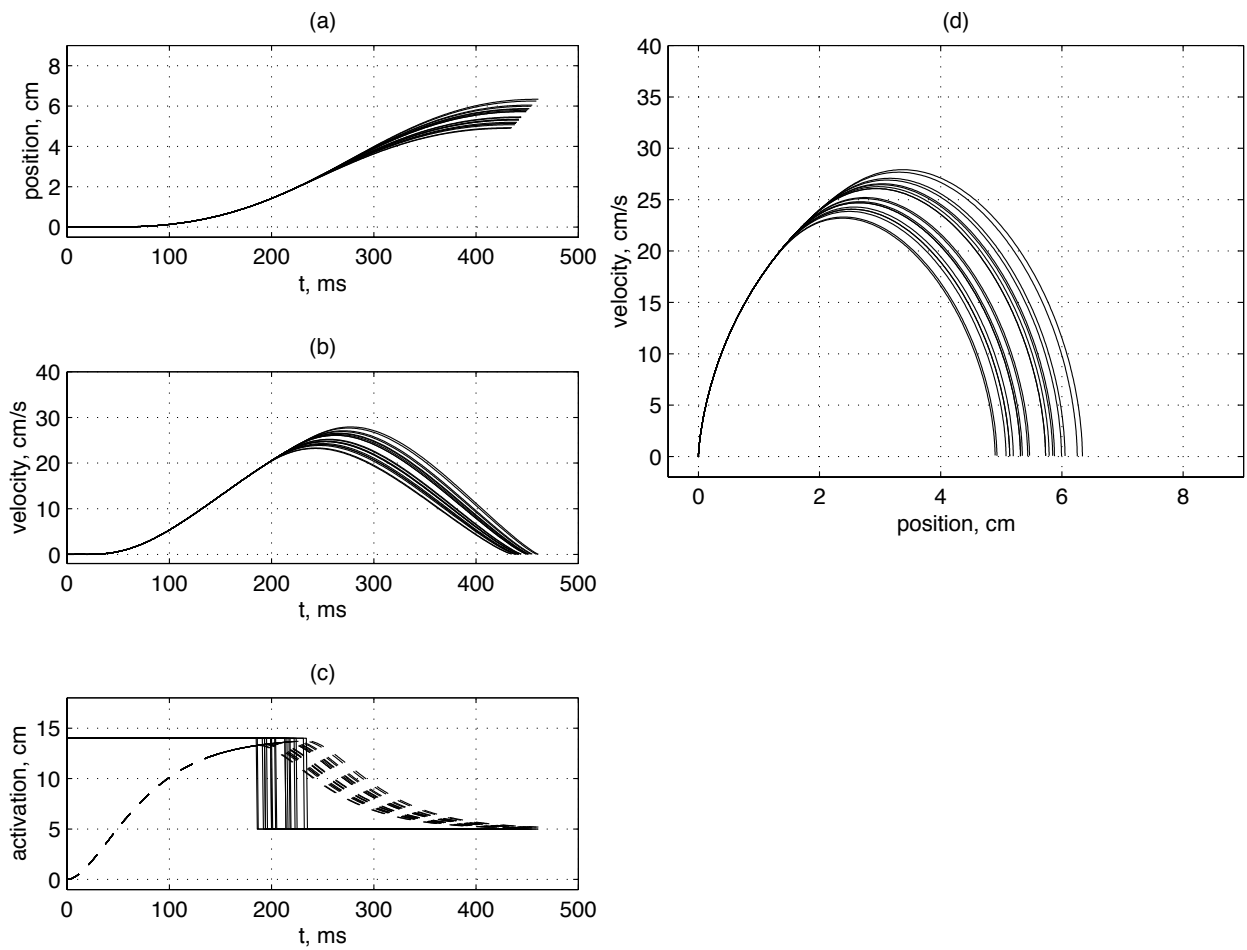
Figure 25: Representative internal movements with stochastic pulse magnitude, system with temporal filtering. Mean pulse magnitude is equal to 14 cm. Panels *(a)*, *(b)*, and *(c)* show, respectively, the movement position, velocity, and the control signal as a function of time. Panel *(d)* shows the phase space trajectories of the movements.

Panels *(b)* and *(e)* in Figure 19 show the fraction of proximal edge movements and the fraction of distal edge movements in different series versus the corresponding pulse magnitude. The dashed line shows the fraction of proximal edge movements, the solid line shows the fraction of distal edge movements. These data provide the criterion used to classify the series as proximal, internal, or distal.

Panels *(c)* and *(f)* in Figure 19 show the minimal final position and maximal final position in different series versus the corresponding pulse magnitude.

Table 2 provides a summarized description of what is shown in every panel of Figure 19 and in other figures of this section. It also provides the numerical data for all the linear fits shown in the figures.

Figure 26 shows how the average velocity of the movements relates to the standard deviation of final positions and to the pulse magnitude. It also shows the same data plotted in terms of equation (2) (see Section 2) which is the generic formulation of Fitts' law. Panels *(a)*, *(b)*, and *(c)* show the data for the system with no temporal filtering. Panels *(d)*, *(e)*, and *(f)* show the data for the system with temporal filtering.

Panels *(a)* and *(d)* in Figure 26 show the average velocity as a function of the pulse magnitude. Similar to the data shown in panels *(a)* and *(d)* in Figure 19, the data from proximal edge series, internal series, and distal series make three separate fits. The corresponding covariance coefficients are shown in Table 2.

Panels *(b)* and *(e)* in Figure 26 show the data in terms of equation (3) (see Section 2), i.e. the standard deviation of the final positions as a function of the average velocity. In this representation the data from proximal series, internal series, and distal series make three separate good linear fits which are very similar to each other. Another salient feature of these data is that for all three of these fits the intercepts are very close to zero. For all practical purposes, the intercepts are equal to zero. The corresponding covariance coefficients and the intercepts are shown in Table 2.

Panels *(c)* and *(f)* in Figure 26 show the average movement time as a function of the index of difficulty (Fitts, 1954), see Section 6.1 above for more details. The proximal series and the distal series make two separate good linear fits. The internal series do not make a good linear fit although the differences between average movement times of internal series are very small compared to those for proximal series or for distal series. Figure 27 shows the same data for the internal series in a finer scale. The covariance coefficients for all Fitts' law linear fits are shown in Table 2.

The stochastic pulse duration data shown in this section produce the same contradiction as the stochastic pulse magnitude data shown in Section 6.1 above. The data make good fits with both Fitts' law relationship and with the linear relationship. This contradiction can be explained in exactly the same way as for the stochastic pulse magnitude data in Section 6.1 above. The reason is that the average velocity computed for each movement separately and then averaged over all movements of a series is not necessary equal to the average movement amplitude divided by the average movement time. Please refer to Section 6.1 above for more details.

Figure 28 shows the average amplitude (9) divided by the average movement time (10) versus the average velocity (8). For the internal series this relationship is the identical one for all practical purposes, while for the proximal and distal series this relationship is substantially nonlinear. The corresponding covariance coefficients, the slope, and intercept values are shown in Table 2.
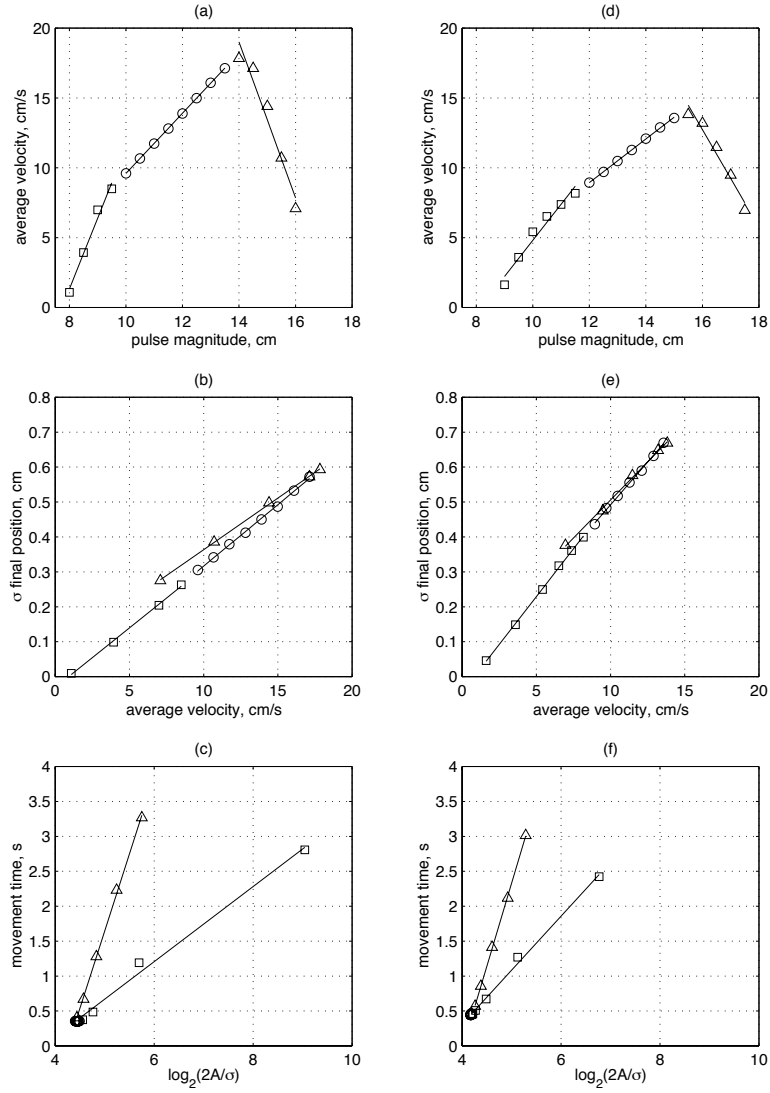
Figure 26: The relationship of the average velocity to the standard deviation of final positions and to the pulse magnitude. *(a,b,c).* Data for the system with no temporal filtering. *(d,e,f).* Data for the system with temporal filtering. *(a,d).* The average velocity as a function of the pulse magnitude. *(b,e).* The standard deviation of the final positions as a function of the average velocity. *(c,f).* The average movement time as a function of the index of difficulty. The data points corresponding to proximal series are shown by squares, points corresponding to internal series are shown by circles, and points corresponding to distal edge series are shown by triangles. The covariance coefficients and intercepts for the linear fits are shown in Table 2.
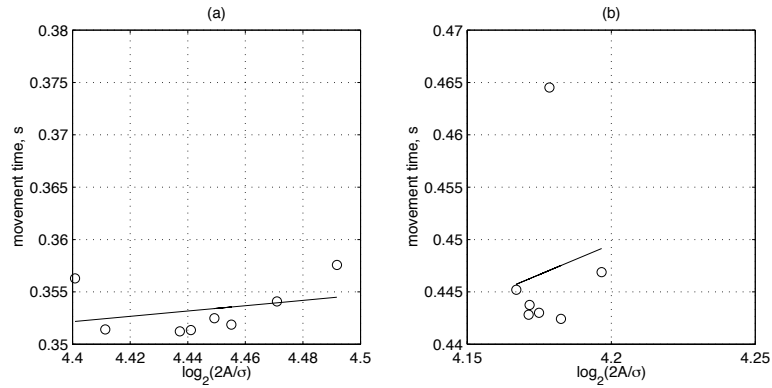
Figure 27: The average movement time as a function of the index of difficulty for internal series of movements. *(a)*. Data for the system with no temporal filtering. *(b)*. Data for the system with temporal filtering. The covariance coefficients for the linear fits are shown in Table 2.
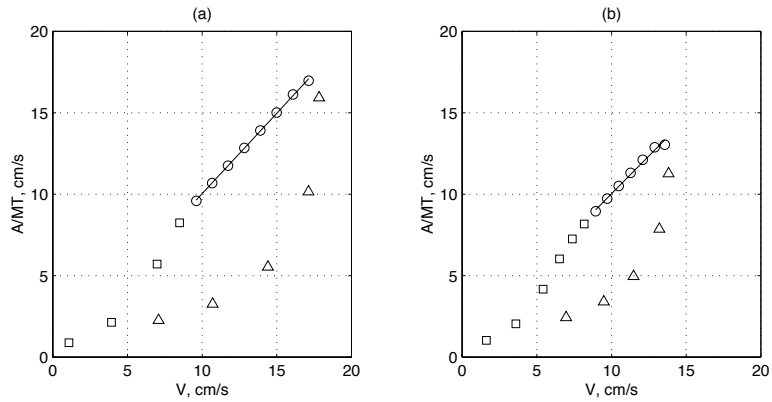

Figure 28: The average amplitude (equation (9)) divided by the average movement time (equation (10)) versus the average velocity (equation (8)). *(a)*. Data for the system with no temporal filtering. *(b)*. Data for the system with temporal filtering. The data points corresponding to proximal series are shown by squares, points corresponding to internal series are shown by circles, and points corresponding to distal edge series are shown by triangles. The covariance coefficients, intercepts, and slopes for the linear fits are shown in Table 2.

6.3 Stochastic plant dynamics

In this set of experiments each series of movements uses a fixed pulse-step combination but the plant dynamics is stochastic. Different series of movements use different pulse magnitude values. The pulse magnitude values were equally spaced every 0.5 cm between 8 cm and 20 cm, so there is a total of 25 series. All the pulse-step combinations had the same step magnitude $u_s = 5$ cm, and the same pulse-duration $\mu(d_p) = 200$ ms.

To simulate stochastic plant dynamics we have perturbed the position of the system every time step of the simulation:

$$x(t + dt) = f[x(t), \dot{x}(t), u(t), dt] + N_t. \tag{12}$$

Here f denotes the numerical simulation function computing position x of system (5) or (7) at time $t + dt$ from state $(x, \dot{x})$ at time t, dt denotes the time step of the numerical integration, N_t denotes the Gaussian noise of zero mean, the value of N_t does not depend on t and is drawn separately for each time step. The fourth order Runge-Kutta was used to compute f in (12). The velocity of the system was then calculated from the perturbed position and position at the previous time step using the Euler approximation:

$$\dot{x}(t + dt) = \frac{x(t + dt) - x(t)}{dt}.$$

The standard deviation $\sigma(N_t)$ of the Gaussian noise N_t is equal to 1 cm/s. For each simulation step over time step dt, the new position $x(t + dt)$ was perturbed according to (12), where

$$N_t \sim \mathcal{N}(0, \sigma(N_t) \cdot dt).$$

This injected noise produces final position spreads that are neither too small, nor too large relative to the size of the stiction region, thus making it possible to observe changes in the final position variance for various pulse magnitudes.

Figure 29 shows the standard deviation of the final position for different pulse magnitudes and the data used to classify movement series as proximal edge series, internal series, and distal edge series. Panels *(a)*, *(b)*, and *(c)* show the data for the system with no temporal filtering. Panels *(d)*, *(e)*, and *(f)* show the data for the system with temporal filtering.

Panels *(a)* and *(d)* in Figure 29 show the final position standard deviation $\sigma(x_f)$ as a function of the pulse magnitude. As in the previous sections, the data points corresponding to proximal edge series are shown by squares, points corresponding to internal series are shown by circles, and points corresponding to distal edge series are shown by triangles.

As one can see in panels *(a)* and *(d)* in Figure 19 the data from internal series make a good linear fit as well as the data from proximal and distal edge series. Each of the three sets of data makes a fit which is substantially different from the two others. The lines in panels *(a)* and *(d)* in Figure 29 show the three linear fits. The corresponding covariance coefficients are shown in Table 3.

The sharp decrease of standard deviations as the pulse magnitude decreases for proximal series is due to the increase in the proportion of proximal edge movements in each new series. Figure 30 shows several representative movements for one of the proximal series for the system with no temporal filtering. Figure 31 shows several representative movements for one of the proximal series for the system with temporal filtering. Analogously, the sharp decrease of standard deviations as the pulse magnitude increases for distal series is due to the increase in the proportion of distal
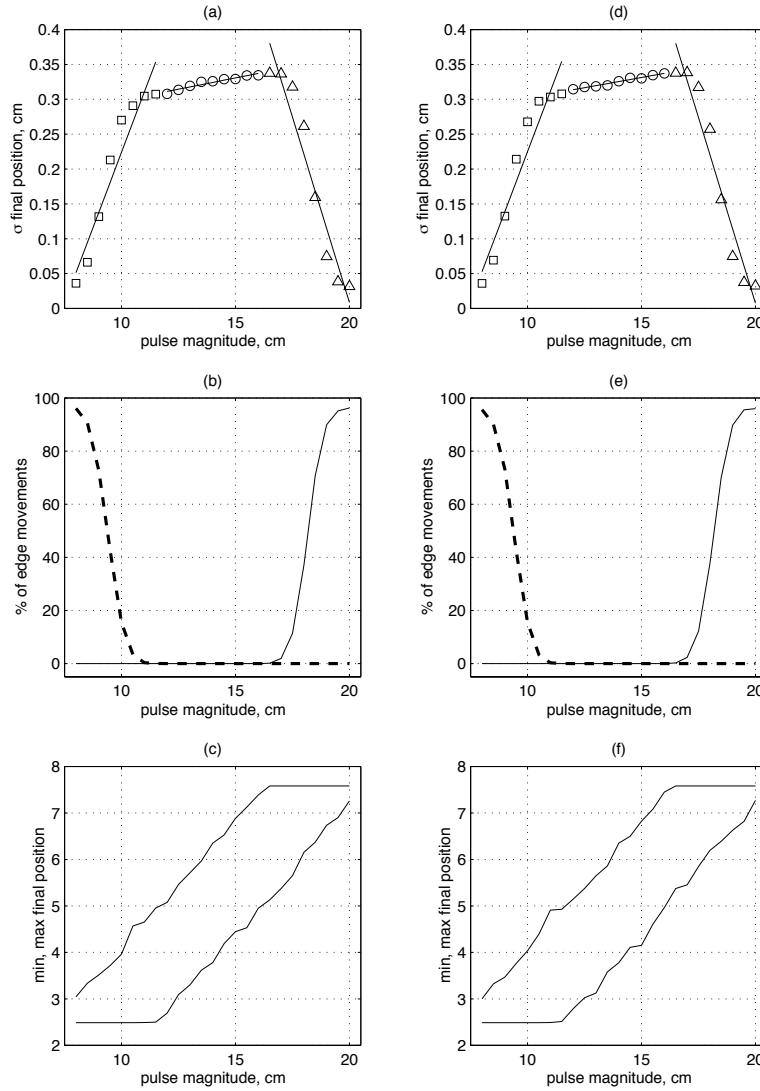
Figure 29: *(a,b,c)*. Data for the system with no temporal filtering. *(d,e,f)*. Data for the system with temporal filtering. *(a,d)*. The standard deviation of final positions as a function of the pulse magnitude. The data points corresponding to proximal series are shown by squares, points corresponding to internal series are shown by circles, and points corresponding to distal edge series are shown by triangles. The covariance coefficients for the linear fits are shown in Table 3. *(b,e)*. The fraction of proximal edge movements and the fraction of distal edge movements in different series as a function of the pulse magnitude. The dashed line shows the fraction of proximal edge movements, the solid line shows the fraction of distal edge movements. *(c,f)*. The minimal final position and maximal final position in different series as a function of the pulse magnitude.

fig	x-axis	y-axis	TF	linear fit parameters		
				proximal	internal	distal
29(a)	u_p	$\sigma(x_f)$	x	$r^2 = 0.92$	$r^2 = 0.93$	$r^2 = 0.94$
(b)	u_p	% of edge movements	x			
(c)	u_p	$\min(x_f), \max(x_f)$	x			
(d)	u_p	$\sigma(x_f)$	v	$r^2 = 0.92$	$r^2 = 0.97$	$r^2 = 0.94$
(e)	u_p	% of edge movements	v			
(f)	u_p	$\min(x_f), \max(x_f)$	v			
36(a)	u_p	V	x	$r^2 = 0.98$	$r^2 = 1.00$	$r^2 = 0.88$
(b)	V	$\sigma(x_f)$	x	$r^2 = 0.97$ $\beta_0 = -0.03$ cm	$r^2 = 0.93$ $\beta_0 = 0.27$ cm	$r^2 = 0.96$ $\beta_0 = -0.08$ cm
(c)	$\log_2\left(\frac{2A}{\sigma}\right)$	MT	x	$r^2 = 0.99$	$r^2 = 0.90$	$r^2 = 0.98$
(d)	u_p	V	v	$r^2 = 0.98$	$r^2 = 1.00$	$r^2 = 0.88$
(e)	V	$\sigma(x_f)$	v	$r^2 = 0.98$ $\beta_0 = -0.03$ cm	$r^2 = 0.97$ $\beta_0 = 0.27$ cm	$r^2 = 0.95$ $\beta_0 = -0.08$ cm
(f)	$\log_2\left(\frac{2A}{\sigma}\right)$	MT	v	$r^2 = 0.99$	$r^2 = 0.94$	$r^2 = 0.98$
37(a)	$\log_2\left(\frac{2A}{\sigma}\right)$	MT	x		$r^2 = 0.90$	
(b)	$\log_2\left(\frac{2A}{\sigma}\right)$	MT	v		$r^2 = 0.94$	
38(a)	V	$\frac{A}{MT}$	x	$r^2 = 0.99$ $\beta_0 = -0.70$ cm/s $\beta_1 = 1.08$	$r^2 = 1.00$ $\beta_0 = -0.02$ cm/s $\beta_1 = 1.00$	$r^2 = 0.95$ $\beta_0 = -1.04$ cm/s $\beta_1 = 1.00$
(b)	V	$\frac{A}{MT}$	v	$r^2 = 0.99$ $\beta_0 = -0.70$ cm/s $\beta_1 = 1.08$	$r^2 = 1.00$ $\beta_0 = 0$ cm/s $\beta_1 = 1.00$	$r^2 = 0.95$ $\beta_0 = -1.02$ cm/s $\beta_1 = 1.00$

Table 3: Summarized description of what is shown in data figures in Section 6.3 and the numerical data for all the linear fits shown in those figures. Field **TF** specifies whether the temporal filtering was applied. Notation β_0, β_1 is used to denote respectively the intercepts and slopes of the linear fits. See text for further explanations.

edge movements in each new series. Figure 32 shows several representative movements for one of the distal series for the system with no temporal filtering. Figure 33 shows several representative movements for one of the distal series for the system with temporal filtering.
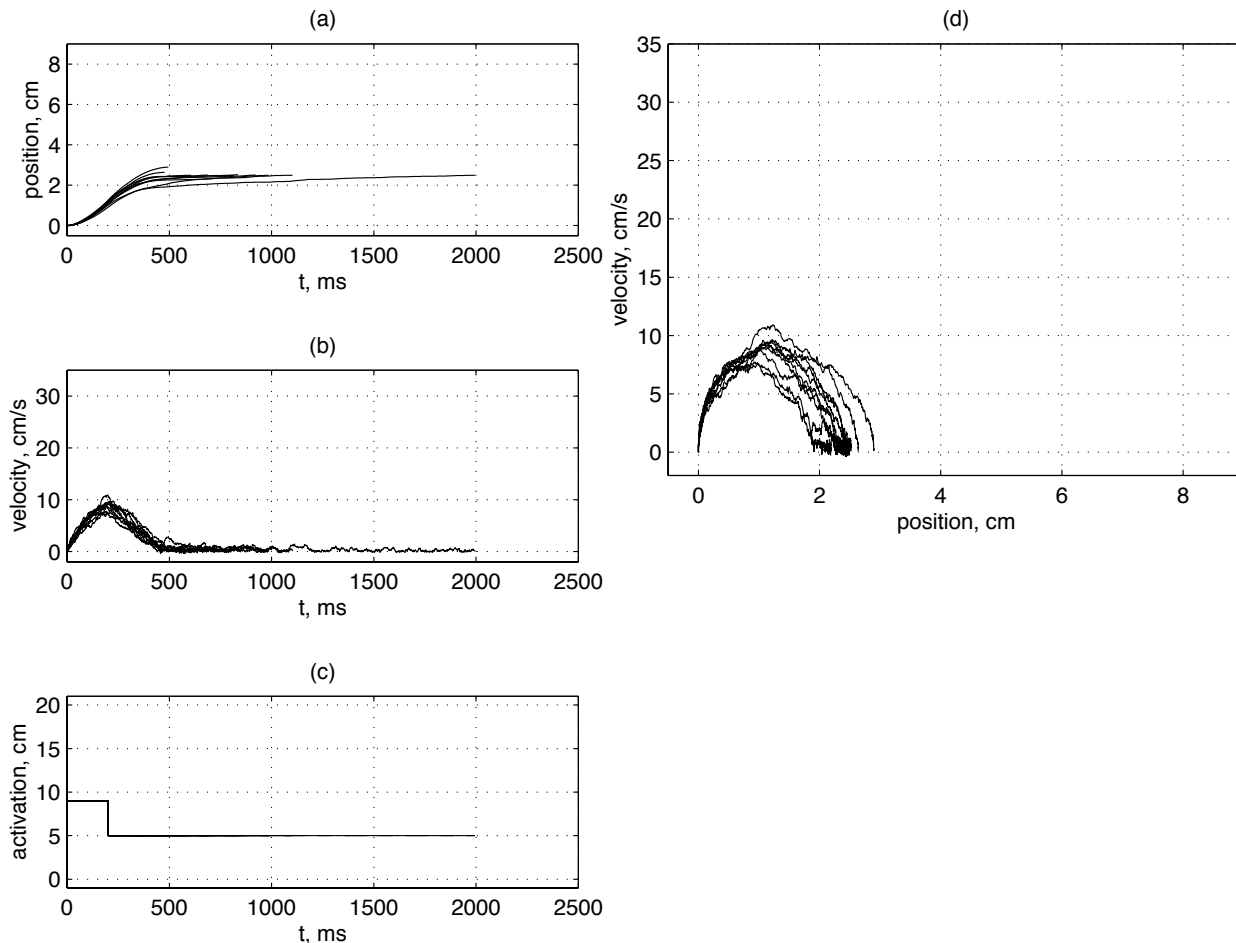

Figure 30: Representative proximal edge movements with stochastic plant dynamics, system with no temporal filtering. Pulse magnitude is equal to 9 cm. Panels *(a)*, *(b)*, and *(c)* show, respectively, the movement position, velocity, and the control signal as a function of time. Panel *(d)* shows the phase space trajectories of the movements.

Figure 34 shows several representative movements for one of the internal series for the system with no temporal filtering. In each of the internal series all the movements terminate in the inner area of the stiction region neither undershooting, nor overshooting it. Figure 35 shows several representative movements for one of the internal series for the system with temporal filtering.

Panels *(b)* and *(e)* in Figure 29 show the fraction of proximal edge movements and the fraction of distal edge movements in different series versus the corresponding pulse magnitude. The dashed line shows the fraction of proximal edge movements, the solid line shows the fraction of distal edge movements. These data provide the criterion for classification of the series as proximal, internal, or distal.
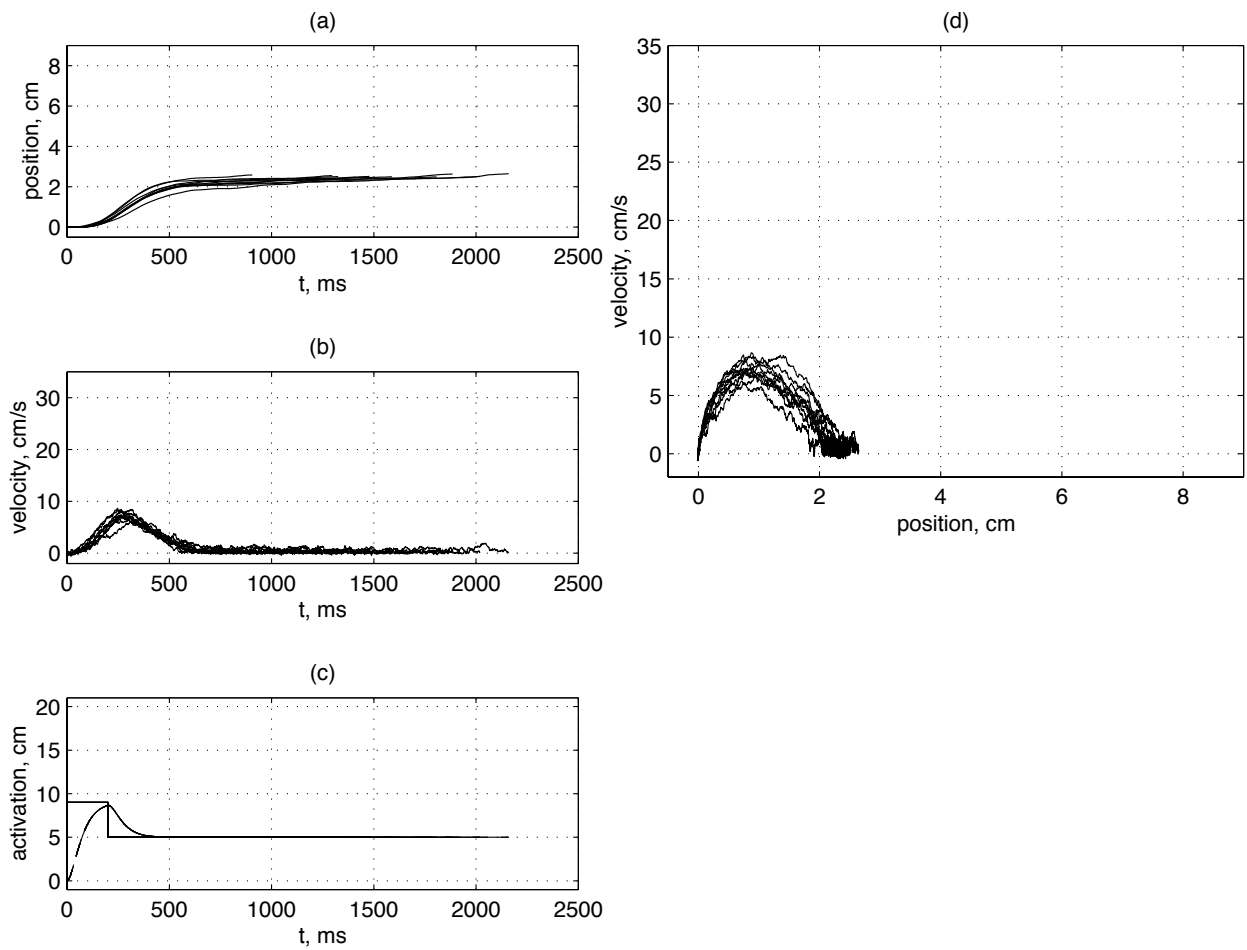
41

Figure 31: Representative proximal edge movements with stochastic plant dynamics, system with temporal filtering. Pulse magnitude is equal to 9 cm. Panels *(a)*, *(b)*, and *(c)* show, respectively, the movement position, velocity, and the control signal as a function of time. Panel *(d)* shows the phase space trajectories of the movements.
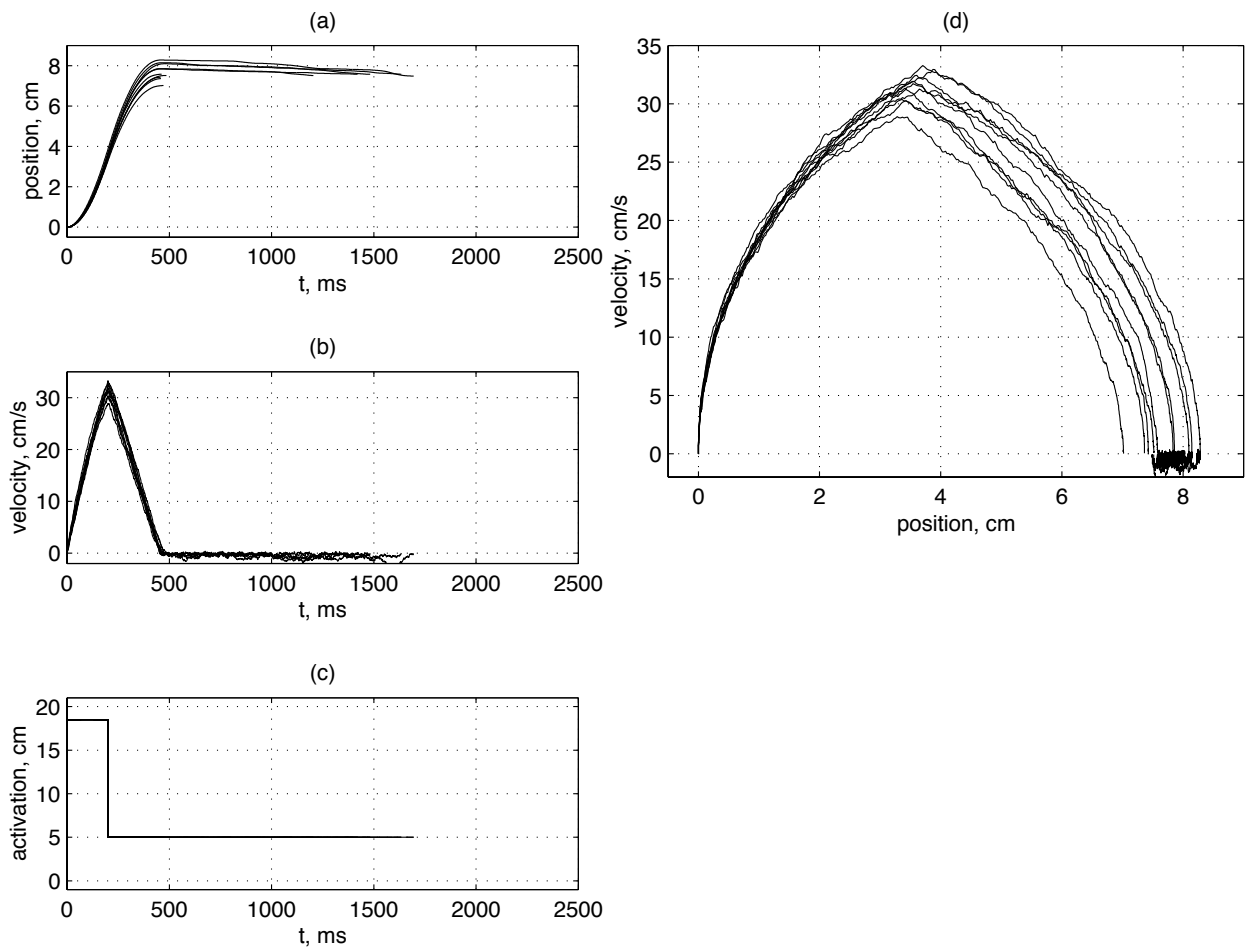
Figure 32: Representative proximal edge movements with stochastic plant dynamics, system with no temporal filtering. Pulse magnitude is equal to 18.5 cm. Panels *(a)*, *(b)*, and *(c)* show, respectively, the movement position, velocity, and the control signal as a function of time. Panel *(d)* shows the phase space trajectories of the movements.

Figure 33: Representative proximal edge movements with stochastic plant dynamics, system with temporal filtering. Pulse magnitude is equal to 20 cm. Panels *(a)*, *(b)*, and *(c)* show, respectively, the movement position, velocity, and the control signal as a function of time. Panel *(d)* shows the phase space trajectories of the movements.
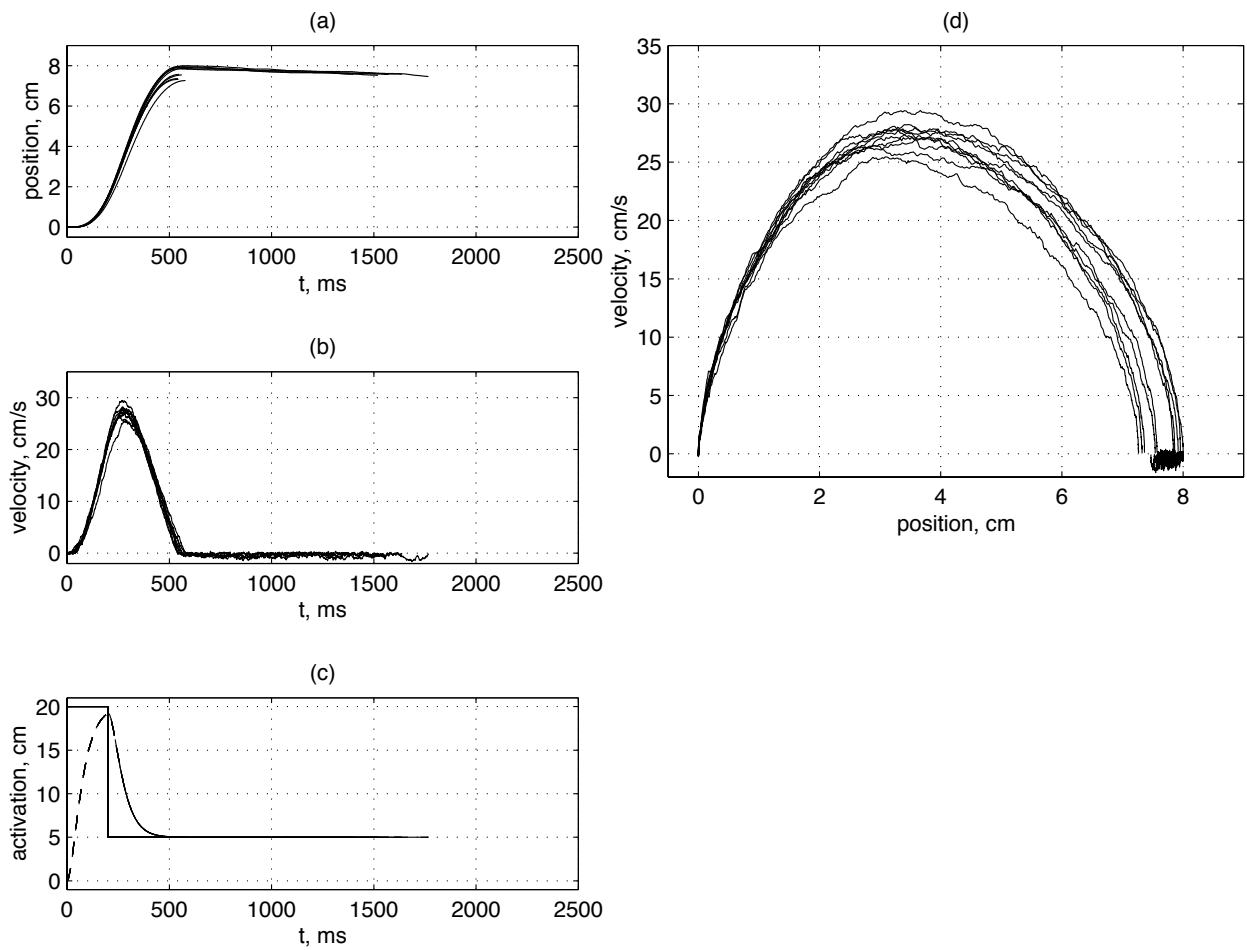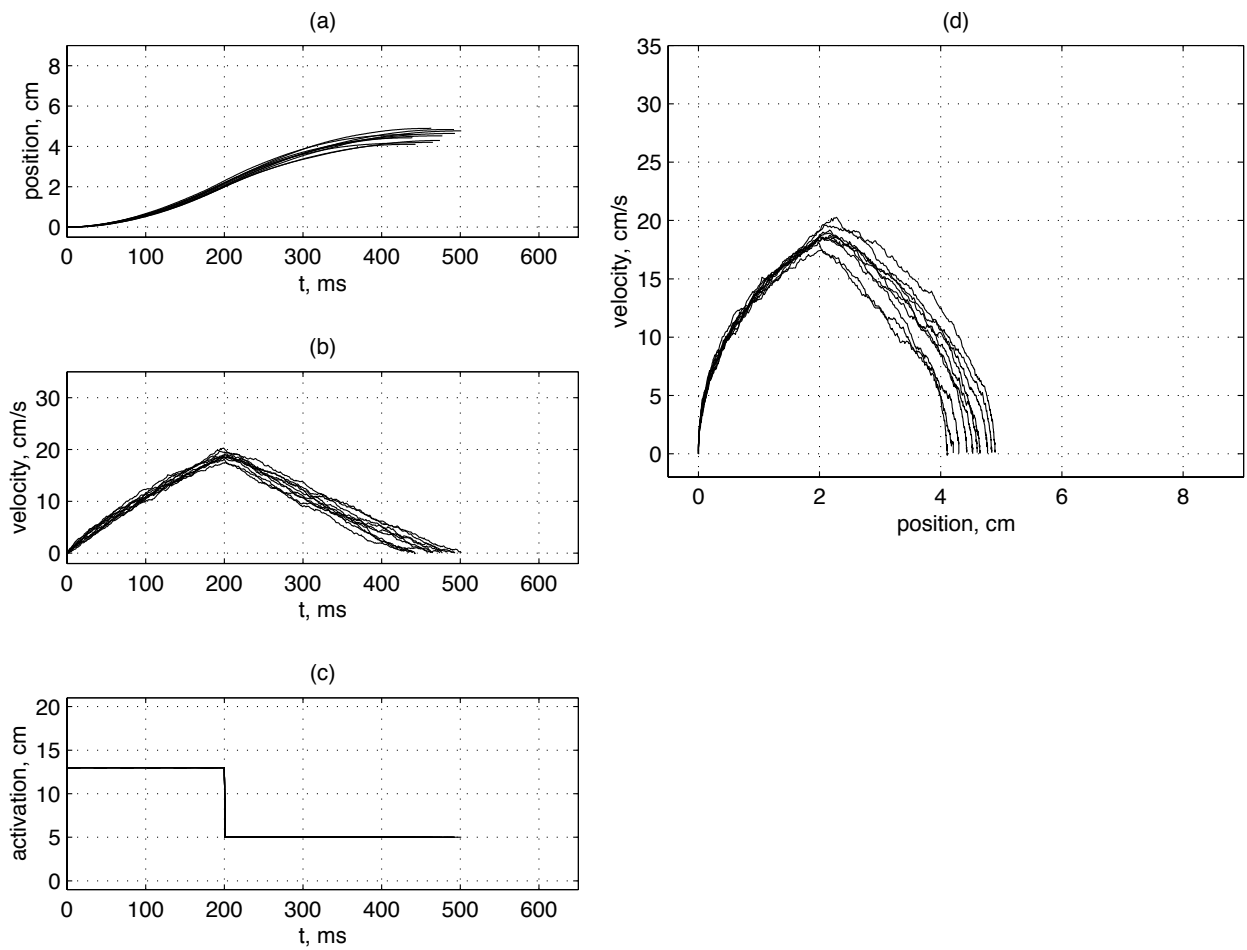
Figure 34: Representative proximal edge movements with stochastic plant dynamics, system with no temporal filtering. Pulse magnitude is equal to 13 cm. Panels *(a)*, *(b)*, and *(c)* show, respectively, the movement position, velocity, and the control signal as a function of time. Panel *(d)* shows the phase space trajectories of the movements.

Figure 35: Representative proximal edge movements with stochastic plant dynamics, system with temporal filtering. Pulse magnitude is equal to 13 cm. Panels *(a)*, *(b)*, and *(c)* show, respectively, the movement position, velocity, and the control signal as a function of time. Panel *(d)* shows the phase space trajectories of the movements.
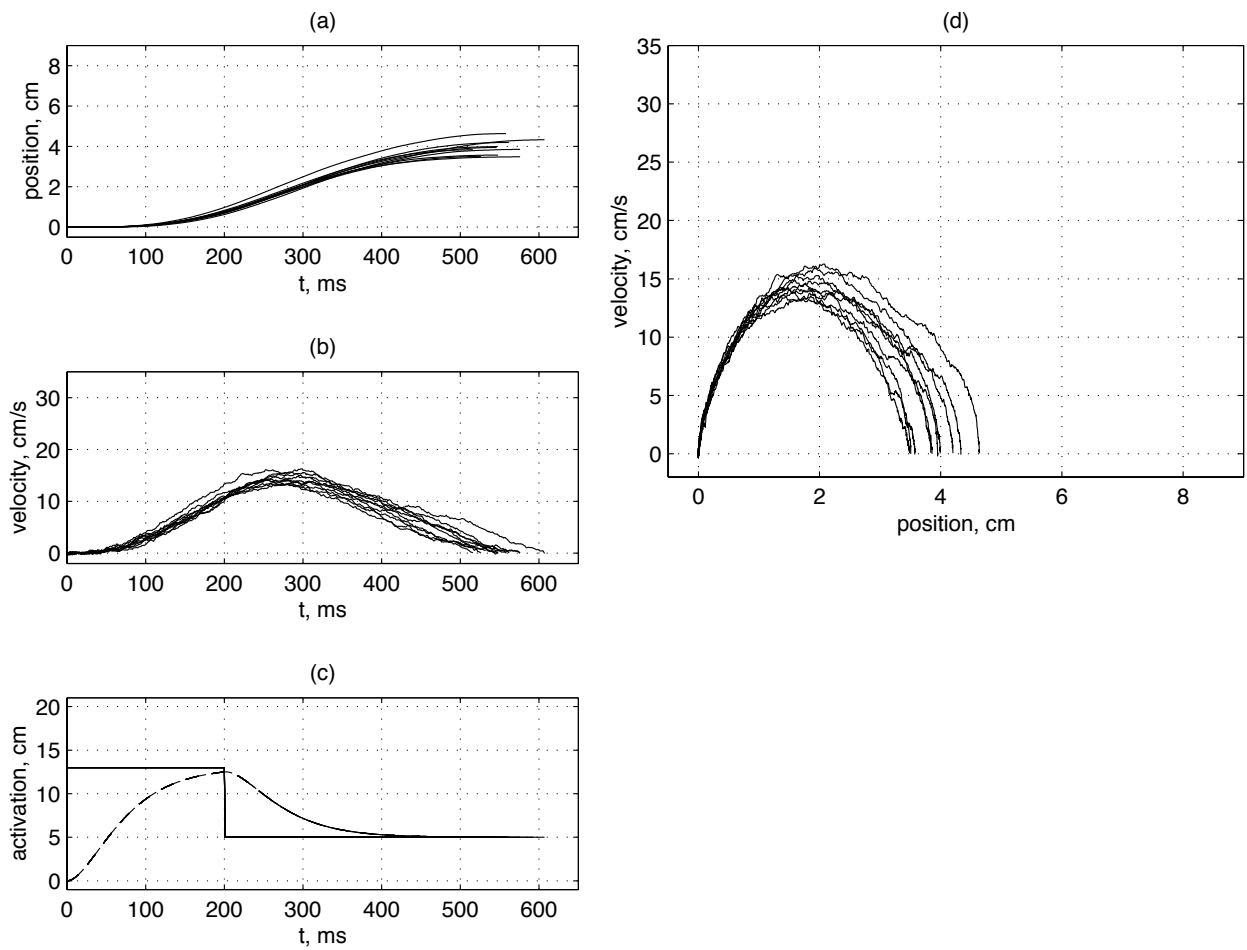
Panels *(c)* and *(f)* in Figure 29 show the minimal final position and maximal final position in different series versus the corresponding pulse magnitude.

Table 3 provides a summarized description of what is shown in every panel of Figure 29 and in other figures of this section. It also provides the numerical data for all the linear fits shown in the figures.

Figure 36 shows how the average velocity of the movements relates to the standard deviation of final positions and to the pulse magnitude. It also shows the same data plotted in terms of equation (2) (see Section 2) which is the generic formulation of Fitts' law. Panels *(a)*, *(b)*, and *(c)* show the data for the system with no temporal filtering. Panels *(d)*, *(e)*, and *(f)* show the data for the system with temporal filtering.

Panels *(a)* and *(d)* in Figure 36 show the average velocity as a function of the pulse magnitude. Similar to the data shown in panels *(a)* and *(d)* in Figure 29 the data from proximal edge series, internal series, and distal series make three separate fits. The corresponding covariance coefficients are shown in Table 3.

Panels *(b)* and *(e)* in Figure 36 show the data in terms of equation (3) (see Section 2), i.e. the standard deviation of the final positions as a function of the average velocity. In this representation the data from proximal series, internal series, and distal series make three separate good linear fits. Another salient feature of these data is that for proximal and distal fits the intercepts are very close to zero. For all practical purposes, the intercepts are equal to zero. The corresponding covariance coefficients and the intercepts are shown in Table 3.

Panels *(c)* and *(f)* in Figure 36 show the average movement time as a function of the index of difficulty (Fitts, 1954), see Section 6.1 above for more details. The proximal series and the distal series make two separate good linear fits. The internal series make a little worse linear fit although the differences between average movement times of internal series are very small compared to those for proximal series or for distal series. Figure 37 shows the same data for the internal series in a finer scale. The covariance coefficients for all Fitts' law linear fits are shown in Table 3.

The stochastic pulse duration data shown in this section bring in the same contradiction as the stochastic pulse magnitude data shown in Section 6.1 above. The data make good fits with both Fitts' law relationship and with the linear relationship. This contradiction can be explained in exactly the same way as for the stochastic pulse magnitude data in Section 6.1 above. The reason is that the average velocity computed for each movement separately and then averaged over all movements of a series is not necessary equal to the average movement amplitude divided by the average movement time. Please refer to Section 6.1 above for more details.

Figure 38 shows the average amplitude (9) divided by the average movement time (10) versus the average velocity (8). For the internal series this relationship is the identical one for all practical purposes, while for the proximal and distal series this relationship is substantially nonlinear. The corresponding covariance coefficients, the slope, and intercept values are shown in Table 3.

7   Discussion

This paper describes a set of computational experiments aimed at studying the movement variability and speed-accuracy trade-off relationship for fast movements with noisy control signal and noisy plant dynamics. In our experiments we used a dynamic model with fractional-power damping. This dynamic model gives rise to a dynamic behavior phenomenon called a stiction region. For each
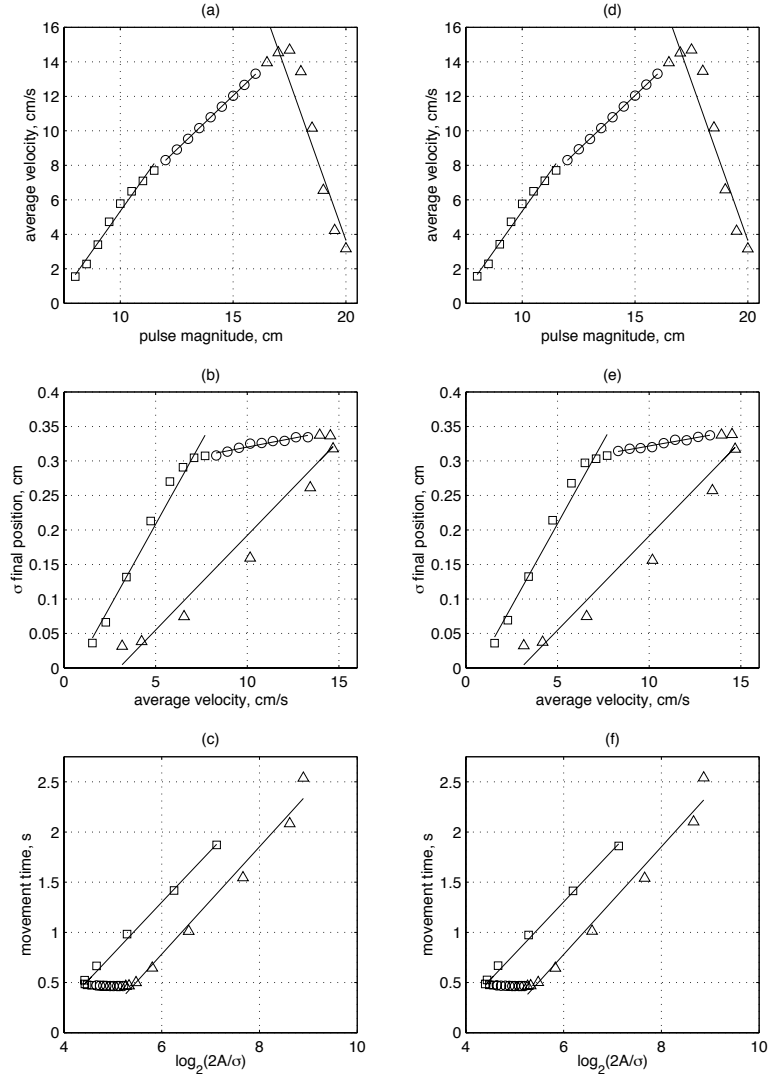
47

Figure 36: The relationship of the average velocity to the standard deviation of final positions and to the pulse magnitude. *(a,b,c)*. Data for the system with no temporal filtering. *(d,e,f)*. Data for the system with temporal filtering. *(a,d)*. The average velocity as a function of the pulse magnitude. *(b,e)*. The standard deviation of the final positions as a function of the average velocity. *(c,f)*. The average movement time as a function of the index of difficulty. The data points corresponding to proximal series are shown by squares, points corresponding to internal series are shown by circles, and points corresponding to distal edge series are shown by triangles. The covariance coefficients and intercepts for the linear fits are shown in Table 3.
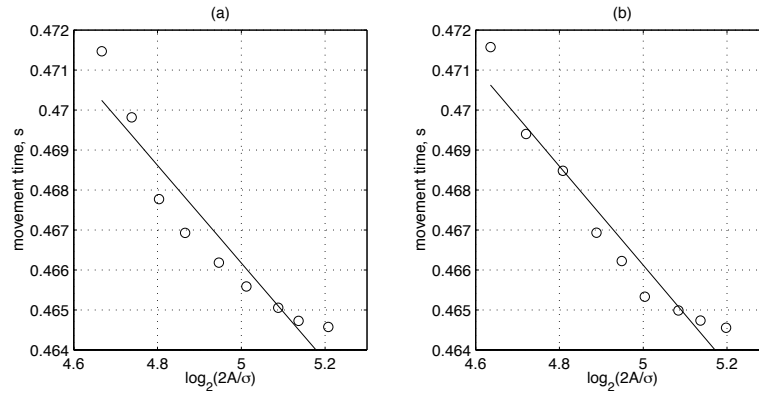
Figure 37: The average movement time as a function of the index of difficulty for internal series of movements. *(a)*. Data for the system with no temporal filtering. *(b)*. Data for the system with temporal filtering. The covariance coefficients for the linear fits are shown in Table 2.
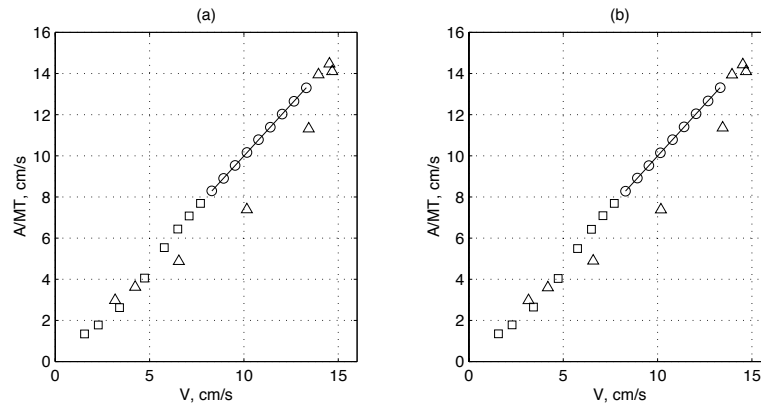
Figure 38: The average amplitude (equation (9)) divided by the average movement time (equation (10)) versus the average velocity (equation (8)). *(a)*. Data for the system with no temporal filtering. *(b)*. Data for the system with temporal filtering. The data points corresponding to proximal series are shown by squares, points corresponding to internal series are shown by circles, and points corresponding to distal edge series are shown by triangles. The covariance coefficients, intercepts, and slopes for the linear fits are shown in Table 2.

49

movement its final position lies within the stiction region, so the final position variability takes place only within the stiction region. Series of movements can have final positions in the inner area of the stiction region or at one of the edges of the stiction region. We call those the internal series and the edge series respectively. These two kinds of movement series produce good separate linear fits, but these two fits are very different from each other. The edge series make a good fit also when plotted in terms of Fitts' law, while the internal series do not.

One of the possible explanations of why both linear and logarithmic (Fitts' law) relationship are observed in the data for edge movement series is that this is an artifact caused by the way the average velocity is computed. When average velocity is computed for each movement and then averaged over all movements in a series, one gets a good linear fit. When amplitudes are averaged over all movements separately from movement times and the amplitude over movement time fraction is used to estimate the average velocity, one gets the nonlinear relationship which makes a good logarithmic fit. This holds true only for edge movement series. For internal movement series both computations give the same result.

Some researchers conducted experiments aimed at distinguishing the conditions or limitations that cause the speed-accuracy relationship to be linear or logarithmic. Schmidt *et al.* (1979) postulated that feedback processing and corrections produced during the movement lead to the logarithmic relationship. Subjects were required to accomplish movements in extremely short time in order to rule out the possibility of any feedback and correction being produced during the movement. For such fast movements a linear relationship was observed. However, this short duration is only short enough to cut off the visual feedback but not the proprioceptive one. Proprioceptive feedback suffices to produce accurate movements as was shown, e.g., by Lackner and Dizio (1994).

Another counterargument to this feedback-corrections theory was suggested by Wright and Meyer (1983). They observed the linear and not the logarithmic relationship for movements of relatively long durations, longer than 500 ms which would suffice to process any kind of feedback. Wright and Meyer (1983) used a different paradigm to produce linear rather than logarithmic relationship. When they enforced subjects to accomplish movements in specified time with high temporal accuracy, the observed relationship was linear. But, when they required high spatial accuracy rather than the temporal one the observed relationship was logarithmic.

The results shown in this paper suggest a new interpretation of this evidence. Probably, in order to accomplish a movement with high spatial accuracy, the stiction region is set to be quite narrow, so that many movements undershoot or overshoot it and then slowly drift towards its nearest edge. In this situation many or all the movements would be edge movements and the logarithmic relationship would be observed. When the temporal accuracy requirement is posed, the stiction region is set to be quite wide and most or all movements terminate in the inner area of the stiction region and the linear speed-accuracy relationship is observed.

We have analyzed only a system with one degree of freedom. In such a system the stiction region is a segment on the position axis, the edges of the stiction region are points, and one can speak about undershooting movements, overshooting movements, and proximal and distal edges of the stiction region. In case of more than one degree of freedom the situation is more complicated, nevertheless the stiction region would have clearly defined borders and one would be able to distinguish between internal movements and edge movements. We speculate that the phenomena described above for the internal and edge movement series would take place for systems with higher number of degrees of freedom.

Appendix   Computing location of the stiction region

This appendix describes the procedure used to compute the stiction region borders for a given activation level u. This computation consists of two parts: a procedure checking for a certain state whether it lies within the stiction region, and a Monte-Carlo algorithm used to generate a set of stiction region states and to determine the borders of the stiction region.

For a given state $(x, \dot{x})$ let us consider a state space trajectory followed by system (5) starting at $(x, \dot{x})$ with the fixed activation level u. State $(x, \dot{x})$ lies within stiction region if during a long time period T the velocity $\dot{x}(t)$, $0 \leq t \leq T$ remains below certain small threshold v_ε. Let us denote by $s(x, \dot{x}, u, t)$ the state of the system at time t if it started from state $(x, \dot{x})$ at time zero and the activation level is equal to u. Let us denote the velocity component of state $s(x, \dot{x}, u, t)$ by $s_v(x, \dot{x}, u, t)$. Let us denote a set of all states within stiction region for activation level u by $\mathcal{S}_u$. Then

$$(x, \dot{x}) \in \mathcal{S}_u \Leftrightarrow \max_{0 \leq t \leq T} s_v(x, \dot{x}, u, t) \leq v_\varepsilon. \tag{13}$$

In our experiments we set $T = 1$ s and $v_\varepsilon = 0.1$ cm/s.

Let us now describe a Monte-Carlo algorithm used to generate a set of stiction region states and to determine the borders of the stiction region. A stiction region is a rectangle in the state space, or a hyper-rectangle in case of more than one degree of freedom, which is aligned with the state space coordinate axes. This rectangle spans small range $[-v_\varepsilon, v_\varepsilon]$ in the velocity dimension. This range is the same for stiction rectangles corresponding to different activation levels u. Let us denote the position range of the stiction rectangle $\mathcal{S}_u$ by $[x_{lu}, x_{ru}]$, where subscripts l and r stand for the lower and upper limits respectively. The exact position range of the stiction rectangle for certain activation level is defined by the following equation:

$$\begin{aligned} x_{lu} &= \min_{(x, \dot{x}) \in \mathcal{S}_u} x, \\ x_{ru} &= \max_{(x, \dot{x}) \in \mathcal{S}_u} x. \end{aligned} \tag{14}$$

The magnitudes of x_{lu} and x_{ru} can be computed by drawing a large number n of states from the entire region of interest in the state space and checking each of the states for belonging to $\mathcal{S}_u$ according to (13):

$$\begin{aligned} x_{lu} &= \min_{(x_i, \dot{x}_i) \in \mathcal{S}_u} x_i, \\ x_{ru} &= \max_{(x_i, \dot{x}_i) \in \mathcal{S}_u} x_i, \end{aligned}$$

where

$$1 \leq i \leq n, \ (x_i, \dot{x}_i) \sim \mathcal{U}\left([x_{\min}, x_{\max}], [-v_\varepsilon, v_\varepsilon]\right).$$

Here $x_{\min}$, $x_{\max}$ denote the position domain borders of the entire region of interest in the state space, and $\sim \mathcal{U}(\ )$ denotes drawing from the uniform distribution. In our experiments we set $n = 10{,}000$, $x_{\min} = 0$ cm, and $x_{\max} = 10$ cm.

References

Abend, W., Bizzi, E., and Morasso, P. (1982). Human arm trajectory formation. *Brain*, 105:331–348.

Abrams, R. A., Meyer, D. E., and Kornblum, S. (1989). Speed and accuracy of saccadic eye movements: Characteristics of impulse variability in the occulomotor system. *Journal of Experimental Psychology: Human Perception and Performance*, 15:529–543.

Barto, A. G., Fagg, A. H., Sitkoff, N., and Houk, J. C. (1999). A cerebellar model of timing and prediction in the control of reaching. *Neural Computation*, 11:565–594.

Brooks, V. B. (1979). Motor program revisited. In Talbott, R. E. and Humphrey, D. R., editors, *Posture and Movement*. Raven.

Bullock, D. and Grossberg, S. (1988). Neural dynamics of planned arm movements: Emergent invariants and speed-accuracy properties during trajectory formation. In Grossberg, S., editor, *Neural Networks and Natural Intelligence*. MIT Press.

Chan, R. B. and Childress, D. S. (1990). On a unifying noise-velocity relationship and information transmission in human-machine systems. *IEEE Transactions on Systems, Man, and Cybernetics*, 20(5):1125–1135.

Connelly, E. M. (1984). A control model: An alternative interpretation of Fitts' law. In *Proceedings of 28th Annual Meeting of the Human Factors Society*, San Antonio, TX.

Corcos, D. M., Gottlieb, G. L., and Agarwal, G. C. (1988). Accuracy constraints upon rapid elbow movements. *Journal of Motor Behavior*, 20:255–272.

Crossman, E. R. F. W. (1956). *The measurement of perceptual load*. PhD thesis, University of Birmingham, England.

Crossman, E. R. F. W. and Goodeve, P. J. (1983). Feedback control of hand-movements and Fitts' law. *Quarterly Journal of Experimental Psychology*, 35A:251–278. Paper presented at the meeting of the Experimental Psychology Society, Oxford, England, July 1963.

Fitts, P. M. (1954). The information capacity of the human motor system in controlling the amplitude of the movement. *Journal of Experimental Psychology*, 47:381–391.

Flash, T. and Hogan, N. (1985). The coordination of arm movements: an experimentally confirmed mathematical model. *Journal of Neuroscience*, 5:1688–1703.

Georgopoulos, A. P., Kalaska, J. F., and Massey, J. T. (1981). Spatial trajectories and reaction times of aimed movements: effects of practice, uncertainty, and change in target location. *Journal of Neurophysiology*, 46:725–743.

Ghez, C. (1979). Contributions of central programs to rapid limb movement in the cat. In Asanuma, H. and Wilson, V. J., editors, *Integration in the Nervous System*, pages 305–320. Igaku-Shoin, Tokyo.

Ghez, C. and Martin, J. H. (1982). Contributions of central programs to rapid limb movement in the cat. iii. agonist-antagonist coupling. *Experimental Brain Research*, 45:115–125.

Gielen, C. C. A. M. and Houk, J. C. (1984). Nonlinear viscosity of human wrist. *Journal of Neurophysiology*, 52(3):553–569.

Gielen, C. C. A. M. and Houk, J. C. (1987). A model of the motor servo: incorporating nonlinear spindle receptor and muscle mechanical properties. *Biological Cybernetics*, 57:217–231.

Gottlieb, G. L. (1993). A computational model of the simplest motor program. *Journal of Motor Behavior*, 25:153–161.

Hogan, N. (1982). Control and coordination of voluntary arm movements. In Rabins, M. J. and Bar-Shalom, Y., editors, *Proceedings of the 1982 American Control Conference*, pages 522–528.

Hogan, N. (1984). An organizing principle for a class of voluntary movements. *Journal of Neuroscience*, 4:2745–2754.

Houk, J. C. (1981). Afferent mechanisms mediating autogenetic reflexes. In Pompeiano, O. and Marsan, C. A., editors, *Brain Mechanisms of Perceptual Awareness*, pages 167–181. Raven.

Houk, J. C., Fagg, A. H., and Barto, A. G. (2001). Fractional power damping model of joint motion. To appear.

Jagacinski, R. J. and Monk, D. L. (1985). Fitts' law in two dimensions with hand and head movements. *Journal of Motor Behavior*, 17:77–95.

Jagacinski, R. J., Repperger, D. W., Moran, M. S., Ward, S. L., and Glass, B. (1980). Fitts'

law and the microstructure of rapid discrete movements. *Journal of Experimental Psychology: Human Perception and Performance*, 6:309–320.

Kawato, M., Maeda, Y., Uno, Y., and Suzuki, R. (1990). Trajectory formation of arm movement by cascade neural network model based on minimum-torque change criterion. *Biological Cybernetics*, 62:275–288.

Keele, S. W. (1968). Movement control in skilled motor performance. *Psychological Bulletin*, 70:387–403.

Kvalseth, T. O. (1975). A model of linear arm movements with preview constraints. *Ergonomics*, 18(5):529–538.

Lackner, J. R. and Dizio, P. (1994). Rapid adaptation to Coriolis force perturbations of arm trajectory. *Journal of Neurophysiology*, 72(1):299–313.

Langolf, G., Chaffin, D. B., and Foulke, J. A. (1976). An investigation of Fitts' law using a wide range of movement amplitudes. *Journal of Motor Behavior*, 8(2):113–128.

Meyer, D. E., Kornblum, S., Abrams, R. A., Wright, C. E., and Smith, J. E. K. (1988). Optimality in human motor performance: ideal control of rapid aimed movements. *Psychological Review*, 95(3):340–370.

Meyer, D. E., Smith, J. E. K., Kornblum, S., Abrams, R. A., and Wright, C. E. (1990). Speed-accuracy tradeoffs in aimed movements: Toward a theory of rapid voluntary action. In Jeannerod, M., editor, *Attention and Performance XIII: Motor Representation and Control*. Erlbaum.

Meyer, D. E., Smith, J. E. K., and Wright, C. E. (1982). Models for the speed and accuracy of aimed movements. *Psychological Review*, 89:449–482.

Miller, L. E. (1984). Reflex stiffness of the human wrist. Master's thesis, Department of Physiology, Northwestern University, Evanston, IL.

Miller, L. E. and Sinkjaer, T. (1998). Primate red nucleus discharge encodes the dynamics of limb muscle activity. *Journal of Neurophysiology*, 80:59–70.

Morasso, P. (1981). Spatial control of arm movements. *Experimental Brain Research*, 42:223–227.

Osu, R., Uno, Y., and Kawato, M. (1997). Possible explanation for trajectory curvature in multijoint arm movements. *Journal of Experimental Psychology: Human Perception and Performance*, 23:890–913.

Partridge, L. D. (1966). Signal-handling characteristics of load-moving skeletal muscle. *American Journal of Physiology*, 210:1178–1191.

Partridge, L. D. (1973). Integration in the central nervous system. In Brown, J. H. U. and Gann, S. S., editors, *Engineering Principles in physiology*, pages 47–98. Academic Press, New York.

Plamondon, R. (1995a). A kinematic theory of rapid human movements: 1. Movement representation and generation. *Biological Cybernetics*, 72:295–307.

Plamondon, R. (1995b). A kinematic theory of rapid human movements: 1. Movement time and control. *Biological Cybernetics*, 72:309–320.

Plamondon, R. and Alimi, A. M. (1997). Speed/accuracy trade-offs in target-directed movements. *Behavioral and Brain Science*, 20:279–349.

Robinson, D. A. (1975). Oculomotor control signals. In Lennerstrand, G. and y Rita, P. B., editors, *Basic Mechanisms of Ocular Mobility and Their Clinical Implications*, pages 337–374. Pergamon Press, Oxford.

Schmidt, R. A., Zelaznik, H., Hawkins, B., Frank, J. S., and Jr., J. T. Q. (1979). Motor-output variability: a theory for the accuracy of rapid motor acts. *Psychological Review*, 86(5):415–451.

Uno, Y., Kawato, M., and Suzuki, R. (1989). Formation and control of optimal trajectory in human multijoint arm movement. *Biological Cybernetics*, 61:89–101.

Woodworth, R. S. (1899). The accuracy of voluntary movement. *Psychological Review (Monograph*

Supplement), 3:1–119.

Wright, C. E. (1983). *Spatial and temporal variability of aimed movements with three contrasting goal points*. PhD thesis, University of Michigan.

Wright, C. E. and Meyer, D. E. (1983). Conditions for a linear speed-accuracy trade-off on aimed movements. *Quarterly Journal of Experimental Psychology*, 35A:279–296.

Wu, C. H., Houk, J. C., Young, K. Y., and Miller, L. E. (1990). Nonlinear damping of limb motion. In Winters, J. M. and Woo, S. L.-Y., editors, *Multiple Muscle Systems: Biomechanics and Movement Organization*, pages 214–235. Springer-Verlag, New York.

Yashin-Flash, T. (1983). *Organizing principles underlying the formation of arm trajectories*. PhD thesis, Massachusetts Institute of Technology.

Zelaznik, H. N., Mone, S., McCabe, G. P., and Thaman, C. (1988). Role of temporal and spatial precision in determining the nature of the speed-accuracy trade-off in aimed-hand movements. *Journal of Experimental Psychology: Human Perception and Performance*, 14:221–230.

Zelaznik, H. N., Shapiro, D. C., and McColsky, D. (1981). Effects of a secondary task on the accuracy of single aiming movements. *Journal of Experimental Psychology: Human Perception and Performance*, 7:1007–1018.